Cooperativity of DNA Object Self-Assembly

Thesis submitted to
The Graduate College of
Marshall University

In Partial Fulfillment of the
Requirements for the Degree of
Master of Science

by

Ava Caudill Dykes

Marshall University

Huntington, West Virginia

July 2001

Marshall University

Department of Chemistry

This thesis was accepted on July 26, 2001

as meeting the research requirements for the master's degree.

Advisor, Department of Chemistry

Member, Department of Chemistry

Member, Department of Chemistry

Dean, Graduate School

This work is dedicated to my children, Jarod and Alec, whose wonder at all things scientific serves as an infinite source of inspiration to me. And to my parents, without whose patience and support continuing my education would not have been possible.

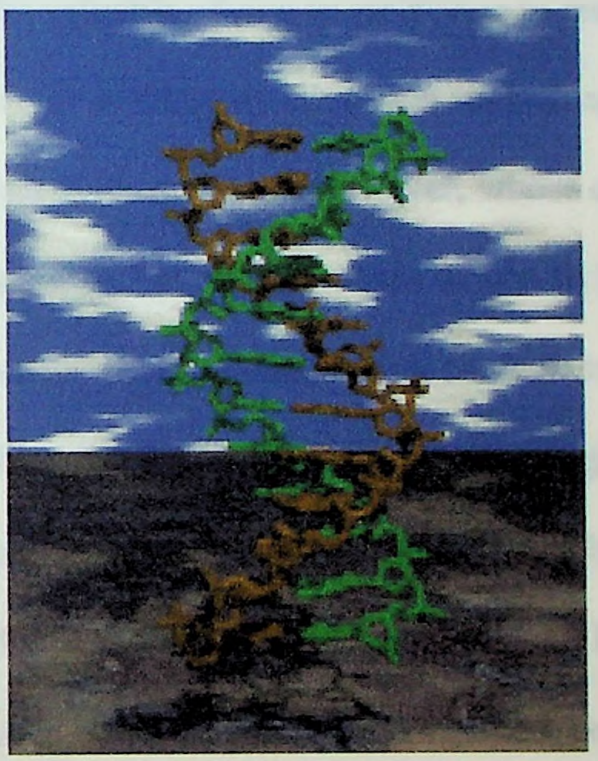

Acknowledgements

Many thanks to Dr. Michael Norton for his continuing support throughout this project. He has gone above and beyond the role of advisor and has become a valued mentor and friend. Dr. Norton's enthusiasm and depth of knowledge have made working for him both challenging and rewarding.

Every member of the Chemistry Department faculty has at some time taken the time to offer valuable advice or assistance to me, and I would like to thank each of them for making my education such an agreeable experience. There are those members, however, whose contributions have been especially memorable: Dr. William Price whom, in his own style of instruction, reinforces concepts by challenging students to view questions from a new perspective; Dr. Robert Morgan, whose insight in the realm of fluorescence spectroscopy has proved invaluable; Dr. John Larson, who was such a help to me when I first entered this program; and Dr. John Hubbard, who made a formidable obstacle, Advanced Organic Chemistry, an enjoyable experience.

List of Tables

List of Figures

ABSTRACT

In this study, the temperature dependence of self-assembling DNA structures was investigated. Specially designed two-dimensional DNA nanoarrays offer not only structural stability not normally associated with DNA, but also provide several possible sites of interaction, referred to as free ends, which can be easily exploited through conventional Watson-Crick base pairing. The ability to synthesize two-dimensional DNA nanoarrays was corroborated by confirming the presence of the nanoarrays by AFM imaging in air. The physical characteristics of two-dimensional DNA nanoarrays were also studied. DNA nanoarray synthesis occurs via a self-assembly process based on Watson-Crick base pairing. This self-assembly occurs through an annealing process, during which stringently coded single-stranded oligonucleotides form duplexes with their conjugates to give rise to a Building Block, the basic unit of these nanoarrays. The blocks in turn are assembled through the base pairing of the free ends to create a full two-dimensional nanoarray. The annealing process was studied to determine the extent of influence neighboring oligonucleotides had on the self-assembly process, a phenomenon referred to as cooperativity. The annealing process was investigated employing available temperature-dependent spectroscopic methods, ultraviolet-visible and fluorescence spectrophotometry. The UV method, which depends on the hypochromic affect, involves monitoring the change in absorbance at 260nm as a function of temperature. The fluorometric method employs an intercalating fluorescent dye whose intensity is multiplies nearly 1000 fold in the presence of double-stranded DNA. This intensity can be measured at a wavelength characteristic to the dye versus temperature to monitor the progress of annealing. An example of a melting curve is shown below, where the

experimental data is shown as □ and a non-linear fit is displayed as X. The melting behavior closely follows a model based on a two-component annealing process, which displays limited cooperativity.

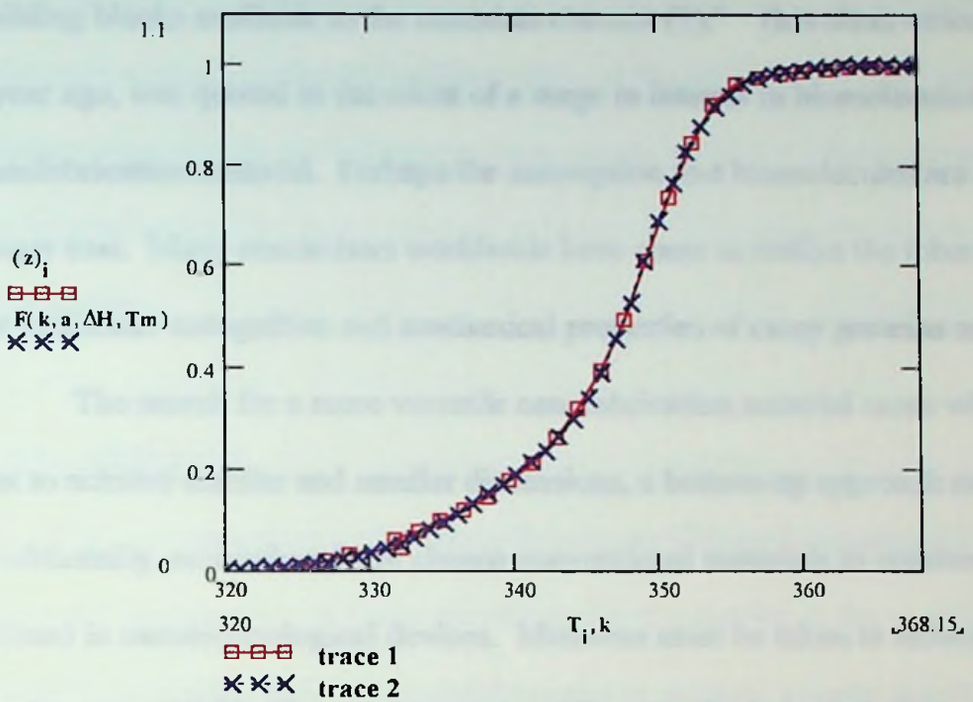

Future work for this study will include the design and implementation of sequences that will employ higher degrees of cooperativity. Higher cooperativity can ensure increased control over the annealing, and therefore, the self-assembly process.

INTRODUCTION: Nanotechnology, Self-Assembly, and Two-Dimensional DNA Nanoarrays

NANOTECHNOLOGY

"Biomolecules are some of the most underused, yet powerful and versatile, building blocks available to the materials chemist (1)." This observation, made less than a year ago, was quoted in the midst of a surge in interest in biomolecules as a nanofabrication material. Perhaps the assumption that biomolecules are underused is no longer true. Many researchers worldwide have come to realize the inherent potential in the molecular-recognition and mechanical properties of many proteins and nucleic acids.

The search for a more versatile nanofabrication material came with the realization that to achieve smaller and smaller dimensions, a bottom-up approach must be employed. Traditionally, researchers have chosen conventional materials to construct objects to be utilized in nanotechnological devices. Measures must be taken to reduce the objects in size by several fold. The most common of these methods is photolithography, frequently used in the semiconductor industry. During microchip production, a wafer of semiconducting material is coated with a photoresistive material. Photolithography is similar to traditional photography, in that a light source, typically a laser, projects an image through a lens system onto this coated wafer, leaving a distinct impression. Photolithography differs from photography in that a photograph is much larger than a negative. In photolithography, the original image being projected onto the wafer is much larger than the area of the wafer the impression occupies (2). This top-down approach not only requires many steps, but also often wastes vast amounts of material and labor. Furthermore, researchers have predicted that they will reach the threshold of the smallest size achievable through this approach within the next few years (3). Antithetically, a

bottom-up approach entails constructing objects from molecular or macromolecular components. Researchers believe that evidence of the success of this approach already exists. For example, within the cells of living organisms chemical structure can be manipulated on the Angstrom scale by enzymatic proteins. The relationship between tasks such as those performed within a cell and the mechanical tasks performed by the existing macroscopic technology has been recognized (4). Mechanisms used by cells can be used as models for developing technology. This area of research is called biomimetics.

SELF-ASSEMBLY

One important trait of a truly efficient nanofabrication material is the ability to undergo self-assembly. A basic definition of self-assembly is the coordinated action of independent entities under non-central control to produce a larger structure or to achieve a desired group effect (5). Many biomolecules have come under study as potential nanofabrication materials because of their ability to self-assemble. Most notable among these are proteins (6), viruses (7, 8), and DNA (9-13). For example, DNA has been studied as a facilitator in the self-assembly of inorganic materials such silver or gold, whose conducting qualities make them useful as electronic components (14, 15). More recently, DNA's ability to self-assemble has shown direct utility in the design and synthesis of two- and three-dimensional DNA objects. The construction of polyhedra, knots, Borromean rings, devices, and two-dimensional crystals of double-crossover, triple-crossover, and Holliday junction parallelograms has been demonstrated (9-13).

TWO-DIMENSIONAL DNA NANOARRAYS

Double-crossover, two-dimensional crystals in particular have shown great promise for utility as a nanofabrication material. These crystals, or nanoarrays, are composed of two distinct repeating double-crossover units, commonly referred to as building blocks. A double-crossover, or DX, structure is one in which two side-by-side, double-stranded helices are linked at two crossover junctions. The positions of these junctions can be coded, or controlled, through conventional Watson-Crick base pairing. Although many different two-dimensional block structures, such as DAO (double-crossover, antiparallel), DPE (double-crossover, parallel, even-spacing), and DPO (double-crossover, parallel, odd-spacing), have been designed, **DAE** units, **D**ouble-crossover, **A**ntiparallel, **E**ven spacing (an even number of half-turns between two crossover junctions), were chosen for nanoarrays synthesis because of their topology. Within a DAE unit, two strands are aligned vertically and two are aligned horizontally, allowing for increased versatility in the design and subsequent reaction of the free ends associated with these strands, as seen in Figures 1 and 2. This design allows for a structural rigidity not normally associated with single- or double-stranded DNA chains (12).

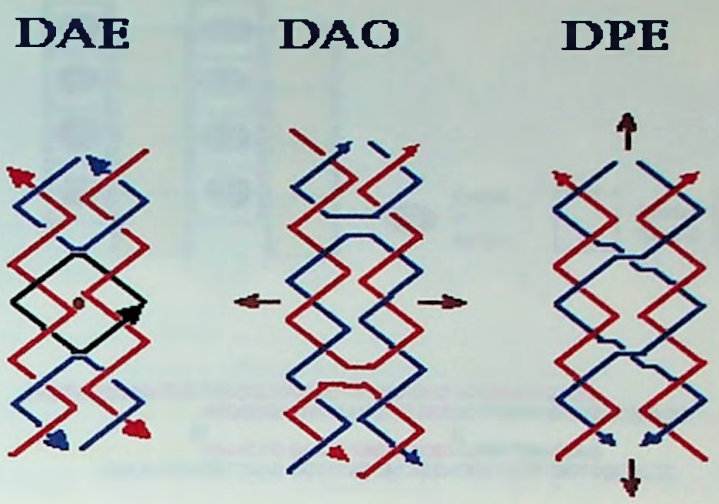

Figure 1: Examples of double-crossover molecules. On the left is an antiparallel evenly spaced unit. The center figure shows an antiparallel structure with odd spacing, and at right, a parallel unit with even spacing can be seen. Arrowheads indicate the 3' ends of the strands. Two consecutive perpendicular lines indicate a full helical turn for a strand (16).

The free ends associated with these structures are the key to their utility. These ends, located on each corner of a DX unit, can be designed so that the bases within code only for some specific substrate, using their exact Watson-Crick base pair compliment. In most cases, the ends code for the free end of the next unit, as shown in Figure 2. It has become possible to use DNA as an easily controllable fabrication material on the nanometer scale.

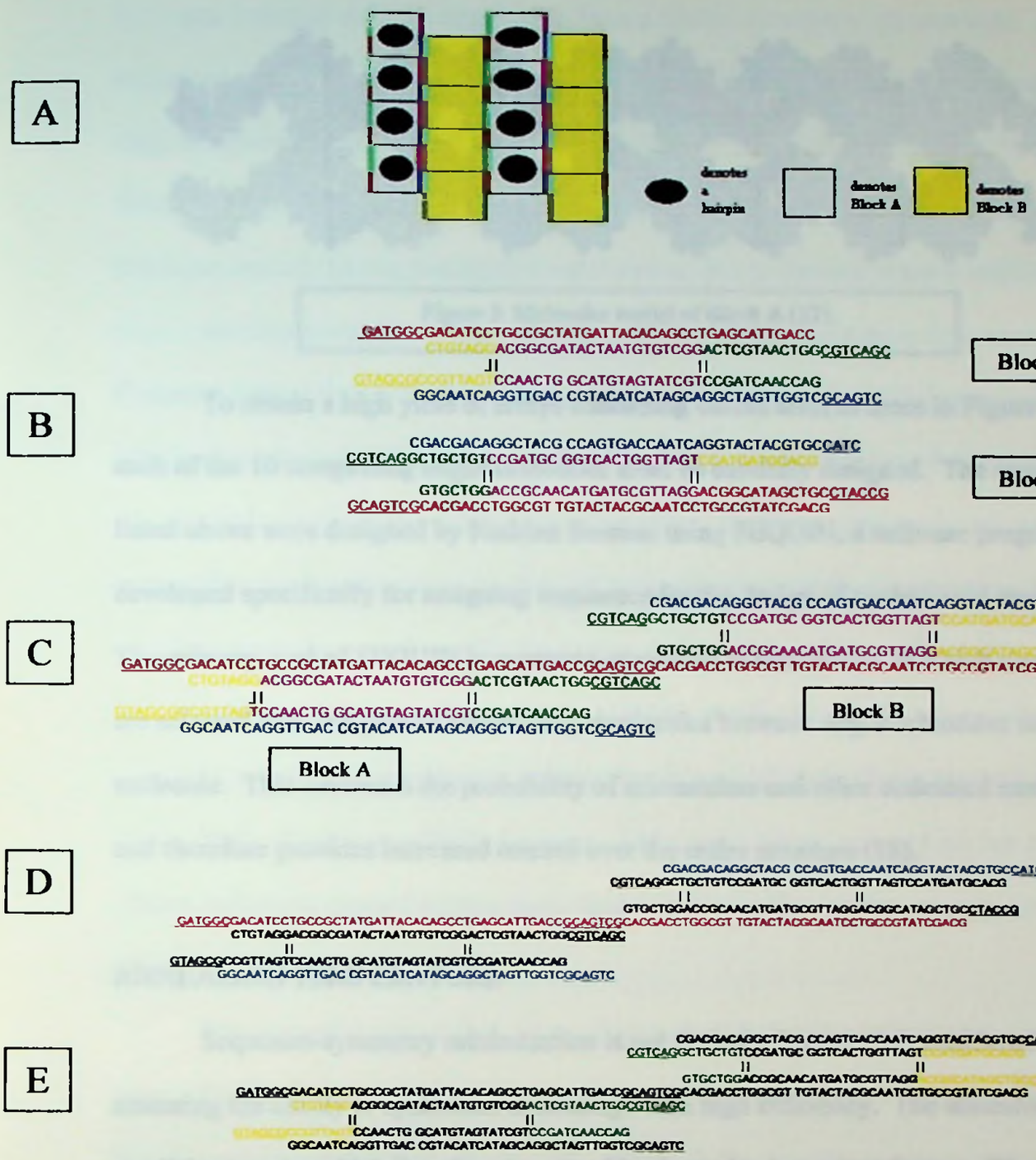

Figure 2: A) Relative position of Blocks A and B within a nanoarray. Free ends are represented as colored bars. **B)** Each block consists of 5 unique oligonucleotide strands. The colors relate the strand's position within a block and are indicative of a correlating sequence between the two blocks. Free ends are underlined for clarification. **C)** Position of Block A in relation to Block B. **D)** Continuity of horizontal strands, red and blue, through a DAE unit. **E)** Continuity of vertical strands, green and yellow, through a DAE unit.

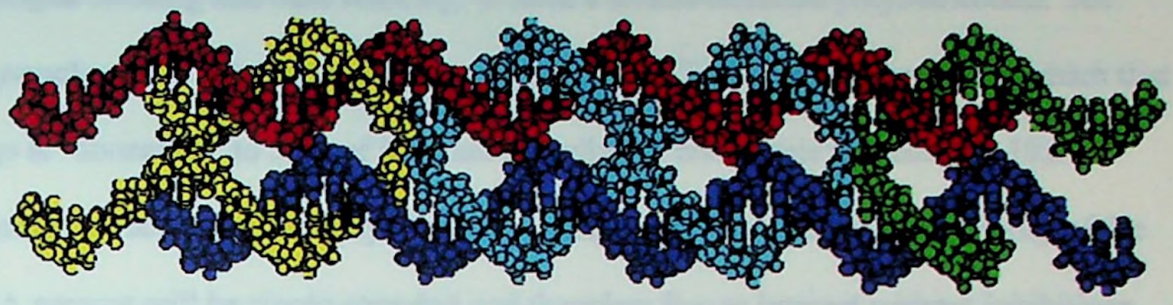

Figure 3: Molecular model of Block A (17).

To obtain a high yield of arrays containing blocks such as those in Figure 2 and 3, each of the 10 comprising oligonucleotides must be carefully designed. The sequences listed above were designed by Nadrian Seeman using SEQUIN, a software program he developed specifically for assigning sequences for the design of nucleic acid structures. The primary goal of SEQUIN is sequence-symmetry minimization, in which sequences are selected with the goal of minimizing similarities between oligonucleotides within the molecule. This decreases the probability of mismatches and other undesired associations and therefore provides increased control over the entire structure (18).

ANNEALING TEMPERATURE

Sequence-symmetry minimization is not the only factor to be considered in assessing the ability to synthesize nanoarrays with high efficiency. The annealing conditions under which the oligos are combined are also important factors. The synthesis of DNA nanoarrays, to be discussed in greater detail below, involves placing the oligonucleotides in solution, heating them to a temperature well above their annealing temperatures, and cooling them at a gradual rate to allow for minimum mismatches during the self-assembly process. Annealing is the pairing of DNA sequences, via

hydrogen bonding and base stacking, to form a double-stranded polynucleotide. An oligonucleotide's annealing temperature, denoted as Ta, is the temperature at which that oligo is "annealed'' to 50% of its exact compliment during this process (18, 19). Heating to a level considerably above this temperature ensures that the majority of the DNA present will be single-stranded and therefore free to interact without inhibitions.

An oligonucleotide's annealing temperature is dependent upon three main factors. Foremost is the oligonucleotide sequence. GC-rich sequences have higher annealing temperatures than do AT-rich sequences. The stronger bonding properties between guanine and cytosine, caused by the presence of an additional hydrogen bond, are responsible for this phenomenon. Second is the oligonucleotide concentration. Higher concentrations are more favorable for duplex, or double-stranded, conformation and therefore promote the annealing process. A third consideration is the salt concentration present in solution. Annealing temperature increases with higher ionic strength due to the steric affects of cations on DNA duplexes. Although different cations may have varying affects, cations in general preferentially bind to a duplex than to two separate single strands of DNA.

The annealing temperature of an oligonucleotide may be estimated in several ways. The three most commonly employed methods are the nearest neighbor method, the %G-C method and the Wallace rule (19). Although Ta, annealing temperature is the correct term, Tm, melting temperature, has become a generic term for the processes of annealing and melting, and so will be utilized within this treatment (20).

The nearest neighbor method employs a thermodynamic basis in its calculations and has given very accurate results. The equation most often used is:

$$Tm := \frac{\Delta H}{\Delta S + R \cdot \ln(C)} - 273.15$$ Equation 1

where ΔH is the sum of the nearest neighbor enthalpy changes, ΔS is the sum of the nearest neighbor entropy changes, R is the gas constant, and C is the total molar concentration of the oligonucleotides.

The % G-C method makes use of the fact that guanine and cytosine are more strongly bonded than are adenine and thymine. The equation utilized in this method neglects the presence of adenine and thymine.

$$Tm = 81.5 + 0.41\ (\%GC) - (500/L) + 16.6 \log (M)$$ Equation 2

where M is the molar concentration of monovalent cations, G and C are the mole fractions of each present, and L is the length of the oligonucleotide. This formula is only applicable to long sequences and does not take nearest-neighbor interactions into account.

Perhaps because of its simplicity, the Wallace rule is the most widely used method. In this method, the annealing temperature is calculated solely on the basis of the number of each base present. The general equation is as follows:

$$Td = 2^{\circ}C \times (A+T) + 4^{\circ}C \times (G+C)$$ Equation 3

where (A+T) is the sum of the number adenine and thymine bases present, and (C+G) is the sum of the number of cytosine and guanine bases present. When specified as Td, the annealing temperature has been calculated as a function of a particular salt and strand concentration. The Wallace rule works best for oligos with 14 - 20 base pairs. It is recommended that 8°C be added to the calculated value for oligos with more than 20 base

pairs to convert Td to Tm. This method should not be used for oligos with more than 50 base pairs.

SPECTROSCOPIC DETERMINATION OF ANNEALING TEMPERATURE

In addition to these methods of estimation, annealing temperatures can be directly determined. The most common techniques are spectroscopic, although other pathways, such as calorimetry or real time PCR thermal cycling, do exist. Ultraviolet-visible spectrophotometry has become the standard for this measurement. A diode array spectrophotometer, such as the Hewlett Packard 8452A used in the present study, operates by passing all wavelengths of light within a set range through a sample. The light is dispersed by a diffraction grating after the sample and the separated wavelengths fall onto different pixels of an array detector (21). This system can be seen in Figure 4.

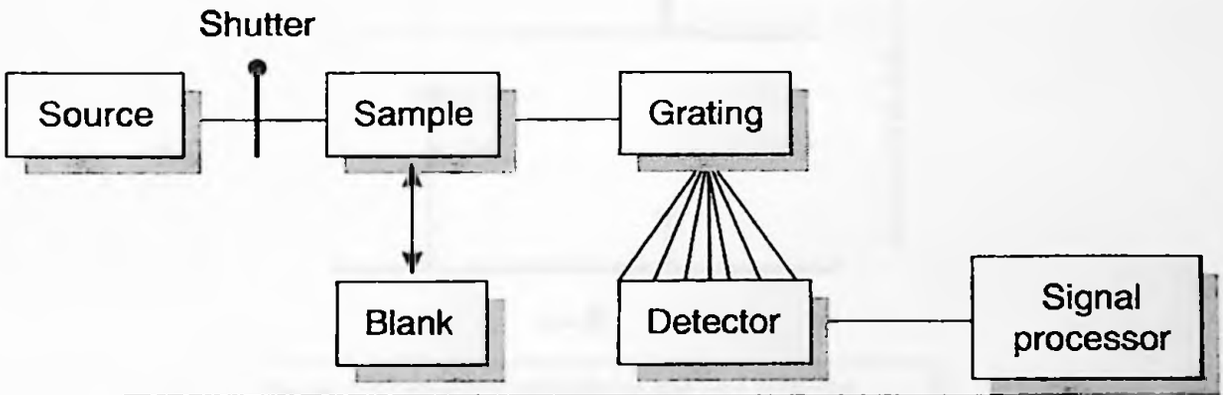

Figure 4: Typical configuration of an ultraviolet-visible absorption spectrophotometer (21).

Annealing curves can be constructed from spectrophotometric data. An annealing curve is a graph of absorbance versus temperature with all points taken at a single wavelength. For DNA studies, based upon the hypochromic effect, this wavelength should be 260nm. The theory behind the hypochromic effect not only states that DNA

absorbs light at 260nm, but goes on to explain single-stranded DNA absorbs light more readily than double-stranded DNA at this wavelength (22). Double-stranded DNA cannot absorb as much light as single-stranded DNA because of interactions between bases, which are stacked while in duplex. The neighboring bases act as non-degenerate chromophores, as shown in Figure 5. The immediacy of the stacked bases allows for Coulombic interactions between them, which causes splitting and rearrangement of intensity. When this rearrangement causes a loss of intensity in the low-energy chromophore, hypochromism results (20). For this reason, it is possible to monitor the conversion of single- to double-stranded conformation through a plot of absorbance at 260nm vs. temperature (23).

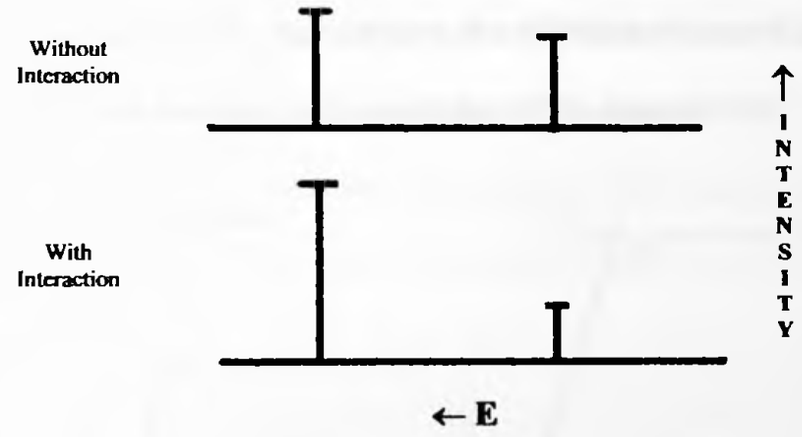

Figure 5: Coulombic interactions between differing chromophores cause splitting and rearrangement of intensity.

A smooth temperature profile could not be achieved directly using the spectrophotometer system available at the time of this study. To obtain temperature values to be used in the construction of an annealing curve, these values had to be determined indirectly using Newton's Law of Cooling. This law states that the rate at

which an object's temperature is changing at any given time is approximately proportional to the difference between its temperature and the temperature of the surrounding medium (24). Newton's Law can be represented mathematically as

$$k \cdot (t_1 - t_2) := -\ln\left(\frac{\theta(t_1) - S}{\theta(t_2) - S}\right) \qquad \text{Equation 4}$$

Where (t_1-t_2) is the time interval to be considered, $\Theta(t_1)$ is the initial temperature, $\Theta(t_2)$ is the final temperature, and S is the temperature of the surroundings, often room temperature.

The annealing temperature can then be derived from such an absorbance vs. temperature plot in several ways. A typical annealing curve, such as in Figure 6, resembles a sigmoid curve. According to the definition of annealing temperature, this temperature should correlate to the midpoint of this sigmoid (25).

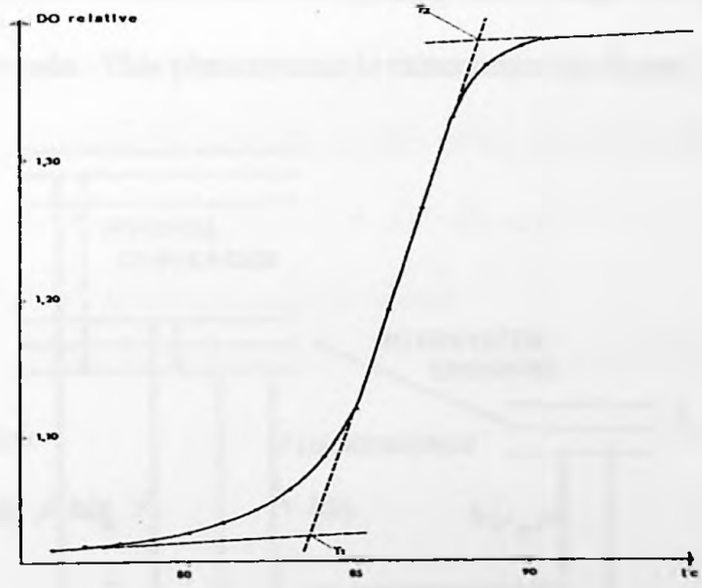

Figure 6: Typical melting curve. Tm can be derived by extrapolating T1 and T2 and applying the following estimate: Tm = (T1+T2)/2.

A similar curve can be obtained using fluorescence spectroscopy. Fluorescence is a form of luminescence, which can be described as the emission of photons from an electronically excited state. Two types of luminescence can be explained, depending on the nature of the ground and excited states. In a singlet excited state, an electron in a higher–energy orbital has the opposite spin orientation of the second electron of the pair, which occupies a lower orbital. In a triplet state, the electrons are unpaired and their spins have the same orientation. In fluorescence, emission results from the return of the high-energy electron of the pair to the lower orbital. Since these electrons have opposite spin orientations, this transition is allowed and the lifetime, which is the average amount of time that a fluorophore remains in the excited state, is typically on the order of 10 nanoseconds. Conversely, phosphorescence occurs when the unpaired electron "falls" from the excited triplet state and returns to a singlet ground state. This transition between states is not allowed and lifetimes are consequently much longer, ranging from milliseconds to seconds. This phenomenon is summarized in Figure 7(26).

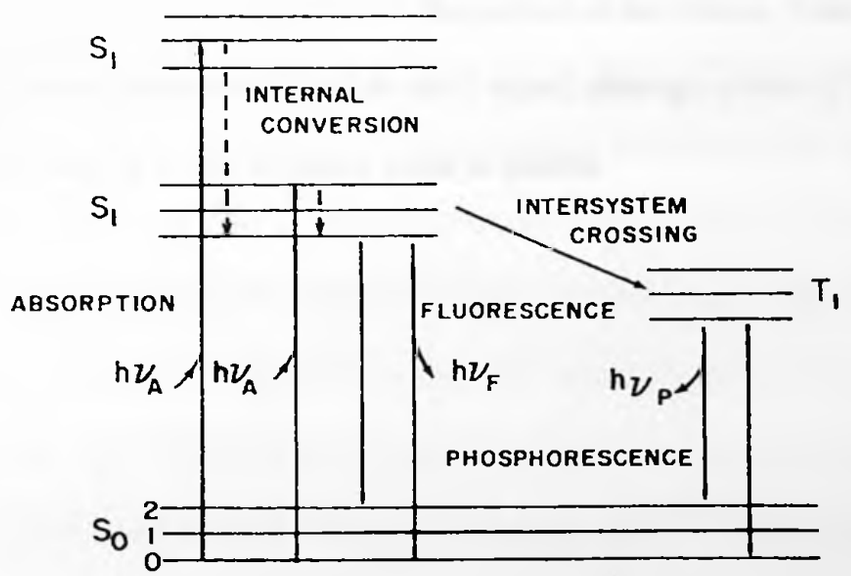

Figure 7: Jablonski diagram. An energy level diagram devised by A. Jablonski to demonstrate luminescent phenomenon (26).

A spectrofluorometer is the instrument commonly used to investigate fluorescence. Most fluorometers consist of a light source, commonly a xenon lamp or a laser, excitation and emission monochromators, reference and emission photo multiplier tubes, and a computerized data acquisition and analysis system. During emission spectra acquisition, white light emitted from the xenon lamp passes through the excitation monochromator, so that only the selected wavelength of light interacts with the sample. The light then is measured by the reference cell. This measurement, referred to as the "R" signal is a measure of the light's wavelength and intensity just before reaching the sample. When the light hits the sample, the fluorophores are excited and light of a characteristic wavelength, longer than that of the excitation wavelength, is emitted. The emitted light is directed to the emission PMT by the emission monochromator where the "S" signal is collected. The S signal gives information on the wavelength and intensity of light at a point in the system after the sample. These signals can be used to evaluate different properties of the sample and diagnostics of the system. Commonly reported spectra contain information based on the S signal, although a ratio of S to R (S/R) is sometimes used as a way to reduce noise in spectra.

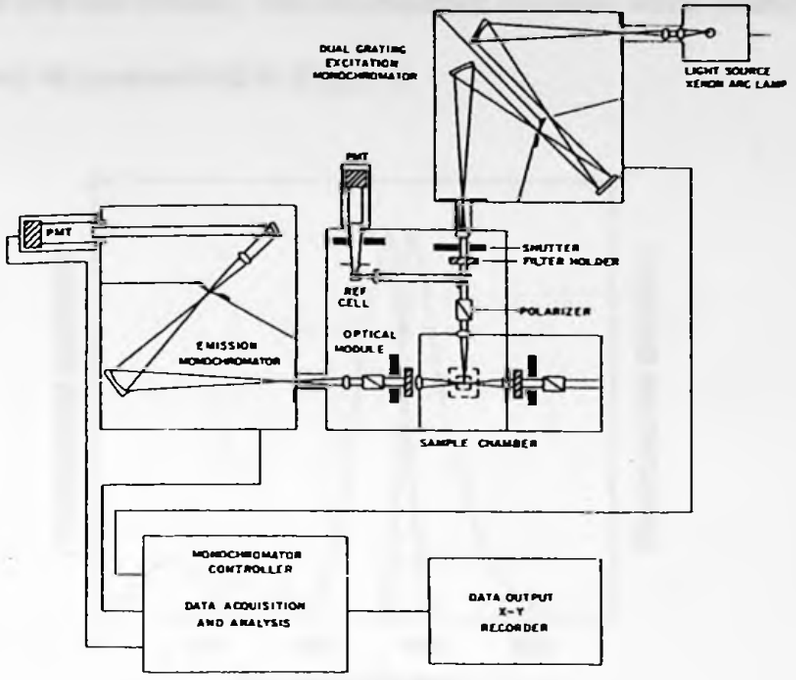

Figure 8: General schematic of a spectrofluorometer. The polarizer and the optical module are used in lifetime studies (26).

To study DNA by fluorescence, a fluorophore must be introduced. Although DNA exhibits a certain amount of intrinsic fluorescence, the amount of material used in this determination did not provide an appreciable amount of signal. Several intercalating dyes were considered for use in this study. An intercalating dye is one that has a planar structure and is able be inserted between two adjacent base pairs in double-stranded DNA. The dye chosen for this study was SYBR Green I (Molecular Probes, Inc.). SYBR Green I is primarily used as a DNA stain for electrophoresis, but was chosen for this solution study because of its increased sensitivity over dyes commonly used for this purpose. Ethidium bromide exhibits 25x less sensitivity than SYBR Green, and its fluorescent enhancement upon binding is a full order of magnitude lower than that of SYBR Green (27). SYBR Green I exhibits a type of selectivity for double-stranded DNA because of this large enhancement, which increases 800 to 1000 fold upon binding (28). SYBR Green I is maximumally excited at 497nm, although characteristic excitation

peaks are present at 290 and 380nm. The fluorescence emission while bound to ds-DNA is centered at 520nm, as summarized in Figure 9.

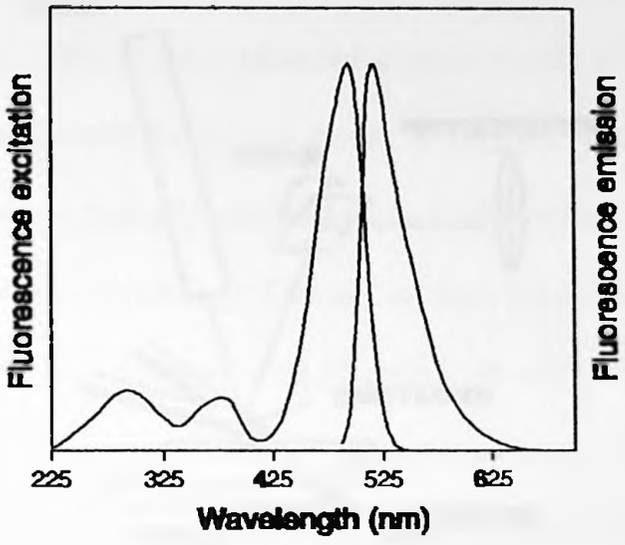

Figure 9: Fluorescence excitation and emission spectra of ds-DNA bound SYBR Green I (28).

ATOMIC FORCE MICROSCOPY

An Atomic Force Microscope, or AFM, is a scanning probe microscope, which is a group of instruments used for studying surface properties of materials from the atomic to the micron level. In this type of microscopy the sample surface is scanned in a rastering pattern. While scanning, the surface is probed with a tiny tip, about 2μm long, which is attached to the free end of a cantilever, measuring between 100 and 200μm long, as can be seen in Figure 10. The cantilever acts as a "diving board," in that repulsive and attractive forces between the tip and the sample surface can cause the cantilever to bend in the same way that a diving board deflects under pressure. Several forces can cause cantilever deflection, although van der Waals forces provide the dominant interaction.

The dependence of the van der Waals force upon the distance between the tip and the sample can be seen in Figure 11 (29).

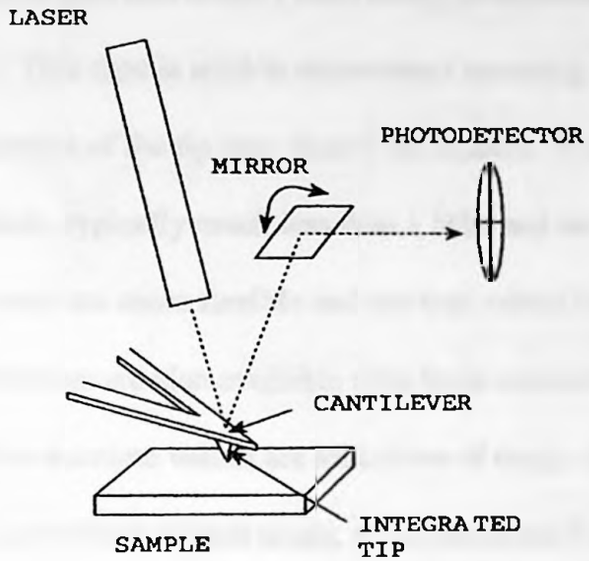

Figure 10: Method of cantilever deflection detection in atomic force microscopy (29).

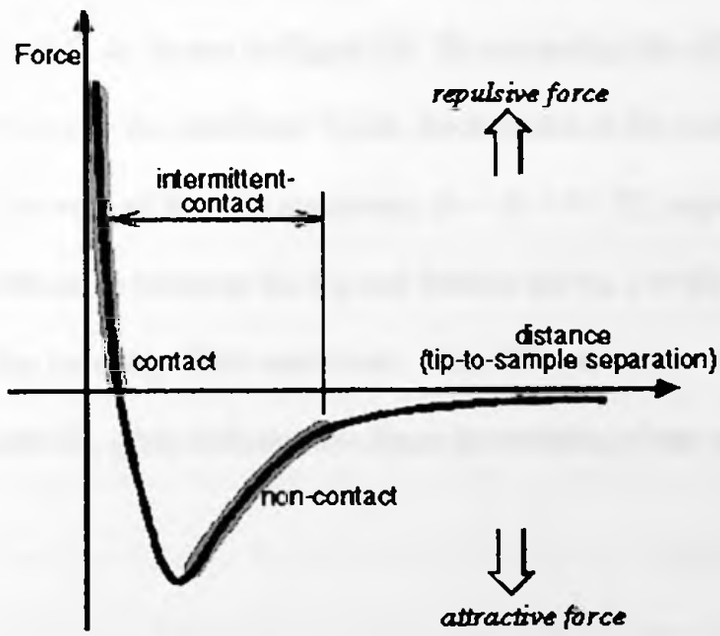

Figure 11: Force-distance curve representing interatomic forces involved in atomic force microscopy (29).

Two main shapes of cantilevers are available, I-shaped and V-shaped. I-shaped cantilevers have a high force constant, usually 30-40 N/m. This high force constant means that the cantilever is stiff and doesn't bend easily in response to changes in sample-tip interactions. This type is used in non-contact scanning, usually applied to soft samples where direct contact of the tip may distort the sample. V-shaped cantilevers have lower force constants, typically much less than 1 N/m and are used in contact mode imaging. These cantilevers are more flexible and are best suited for imaging hard samples. I-shaped cantilevers are also available with force constants with values between 1 and 20 N/m. These intermediate values are indicative of range of flexibility that may be used in tapping or intermittent-contact mode, to be discussed below.

During scanning, a laser spot is positioned on the reflective end of the cantilever. Light from the cantilever is directed by a mirror onto a split photo-diode divided into quadrants A, B, C, and D, as shown in Figure 10. By measuring the difference in signals between these quadrants as the cantilever bends, fluctuations of the cantilever position can be measured. The sum of the four quadrants, (A + B + C+ D), represents the total laser signal. The difference between the top and bottom halves, (A+B) – (C+D), gives information about the bending of the cantilever. The difference between the right and left halves, (A+C)-(B+D), gives information about the twisting of the cantilever.

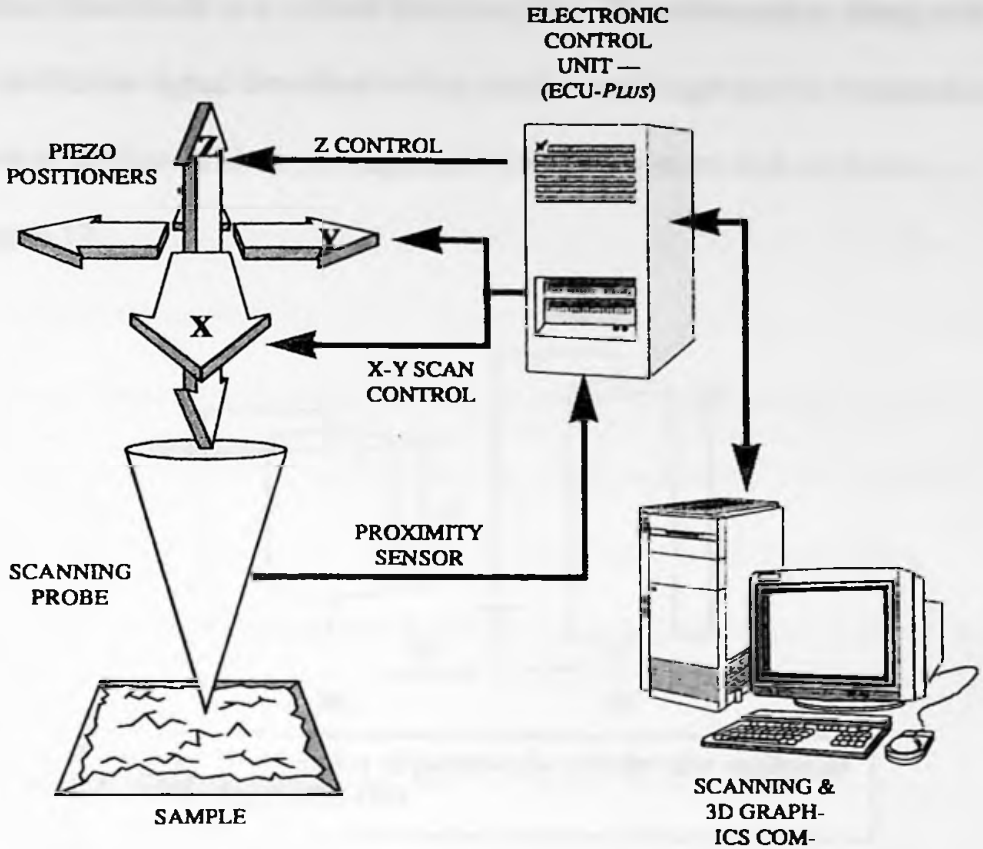

Figure 12: Generalized schematic of scanning probe microscope operation (30).

Surface position is controlled through the use of piezoelectric scanners. Piezoelectric ceramics are a class of materials whose physical dimensions change in the presence of an electric field. During scanning, an electric potential is applied across electrodes on opposing faces of the material. The material, usually cylindrical in shape, becomes elongated and the diameter shrinks when this voltage is applied, as seen in Figure 13. These changes in dimension are the basis for the design of the tripod scanner. Tripod scanners are composed of three such piezoelectric cylinders, mounted orthogonally, as in Figure 14. As voltage is applied to the X and-or Y piezo, they push against the base of the Z piezo and cause it to move laterally. Applying voltage to the Z

piezo itself causes movement in a vertical direction (30). This information, along with the cantilever deflection signal described earlier, can be used to generate a topographical map of the sample surface. This is accomplished through a system such as the one pictured in Figure 12.

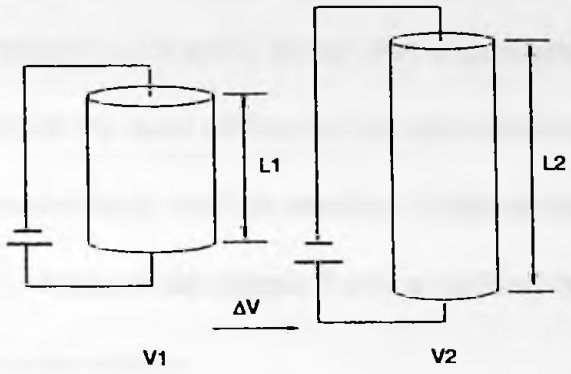

Figure 13: Alteration of piezoelectric cylinder after application of electric potential (30).

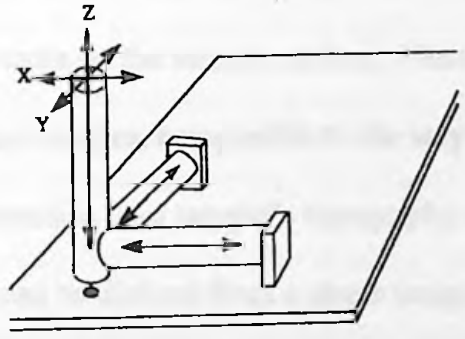

Figure 14: Tripod scanner configuration (30).

There are three general modes in which an AFM is operated. In contact mode, the sample and the tip are in "contact" as the sample is being scanned. They are so close that inter-molecular forces of the tip and the sample are repulsive. Unfortunately, this sort of contact creates large lateral forces on the sample as the tip is being "dragged" across it. These forces often include friction and can interfere with the signal, depending on the

type of sample being scanned. In tapping, or intermittent-contact, mode the cantilever oscillates very rapidly near the surface at a characteristic resonant frequency. This way the tip is only in contact with the sample for a very small amount of time (a fraction of its oscillation period), and lateral forces are greatly reduced. In non-contact mode, the cantilever is oscillated far enough above the sample so that the inter-molecular forces are no longer repulsive. These attractive-repulsive forces were summarized in Figure 8. Non-contact mode is considered the most difficult of the three modes. This is partially due to the ease of water contamination, and the resulting "jump-to-contact" effect observed when water on the surface of the sample forms a capillary bridge with the tip and imaging is forced into contact mode.

An AFM imaging mode that can be used is phase detection. In phase imaging, the phase lag between the resonant frequency driving the cantilever and the detected oscillation signal response is monitored, as shown in Figure 15. These phase differences are indicative of viscosity differences on the sample surface. Phase shifts are registered as bright and dark regions in phase images, comparable to the way height changes are indicated in height images. Information on a sample's topography as well as its elasticity, adhesion and friction properties can be derived from a phase image simultaneously.

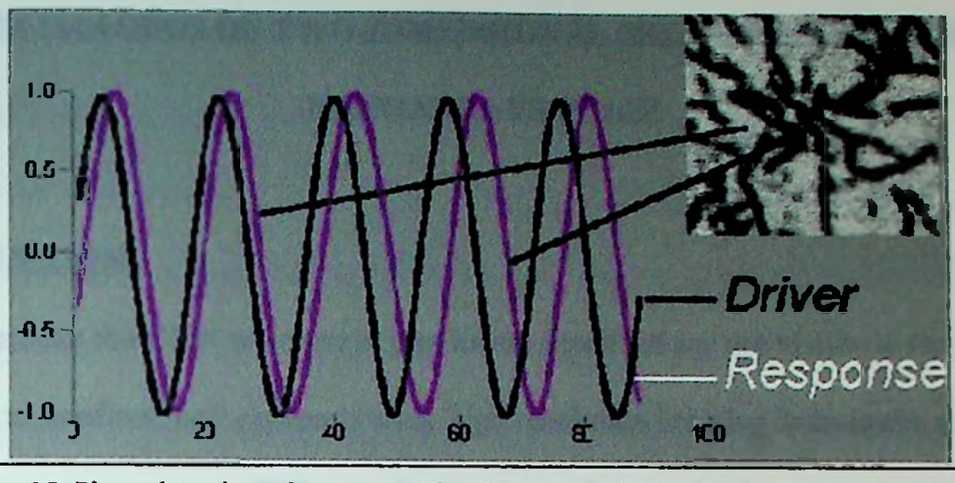

Figure 15: Phase detection microscopy. The phase lag varies in response to the mechanical properties of the sample surface (31).

COOPERATIVITY

The way in which the oligonucleotides bind to each other during the annealing process in "normal" DNA base pairs depends upon their complimentarity. However, for DNA object assembly a thorough understanding of cooperativity is also essential. Cooperative binding occurs when the binding of a ligand to a site on a molecule influences the affinity of other sites for the same kind of ligand. Cooperativity can either be classified as positive, when affinity is increased, or negative, when affinity is decreased. Cooperativity can also be described using the concept of allostery. An allosteric molecule is one whose topologically distinct binding sites interact functionally with each other. Homeoallestery occurs when ligand binding affects the binding of ligands of the same type (20).

At present, an annealing period of 48 hours is required to manufacture even a small amount of DNA nanoarray material. A better understanding of the mechanism of the self-assembly process involved will lead to the development of faster, more efficient, and more effective assembly pathways. This in turn can lead to extensive utilization of DNA objects in the rapidly growing field of nanotechnology.

AFM IMAGING OF TWO-DIMENSIONAL SELF-ASSEMBLED DNA NANOARRAYS IN AIR

INTRODUCTION

Because the DNA nanoarrays previously described are not visible to the eye, it is necessary to confirm their presence using high resolution imaging techniques, namely atomic force microscopy. DX crystals have been characterized previously attached to mica under isopropanol by atomic force microscopy, or AFM (12). Because the use of a fluid cell is not always convenient, a sample preparation method for imaging in air was developed. Stringent sample preparation conditions and imaging parameters were used to obtain high quality AFM images of DX crystals in air. Imaging DNA in air presents challenges not encountered in solution studies, chiefly salt deposition and hydration effects. Salt deposits can be minimized by alternately rinsing and drying the samples. Successful imaging of the DNA in the presence of a hydration layer (i.e. contamination or water layer) is accomplished by operating in intermittent contact mode. The delicate nature of this sample requires the use of low drive amplitudes, high set-point amplitude ratios, and low force constant cantilevers.

DNA NANOARRAY PREPARATION

Based upon the protocol described in Winfree et al. (11), a 10mM TAE Mg^{+2} buffer was prepared (4.0ml of 1M *tris*-HCl, 0.2ml of 500mM EDTA, 60µl of 5M NaCl, 1.0ml of 1M $MgCl_2$, 94.74ml 10.1 MΩ-cm nanopure water). To denature any DNase

impurity, the buffer was placed in a Hiclave HV-110 autoclave at 125°C for 20 minutes. The final pH of the finished buffer was 8.13.

Under a laminar flow hood, 50µl of the TAE buffer was added to 200pmol each of 10 oligonucleotides contained in 1.5ml microfuge tubes. These oligonucleotides, a gift from the laboratory of Dr. Nadrian Seeman of New York University, were synthesized using standard methods. The specific sequences are designated in Figure 16, beginning at the 5' end. The resulting suspensions were then mixed thoroughly using a Fischer Vortex Genie 2. Using a fresh pipette tip for each oligonucleotide, 5µl of each 4.0 pmol/µl solution were systematically taken from each container and added to a freshly autoclaved 1.5ml microfuge tube. This gave a final volume in the new microfuge tube of 50µl.

This microfuge tube was placed in a 2.0L-water bath that had been warmed to 50°C. The water bath was heated to 94°C and maintained at this temperature for 3 minutes. After this equilibration period, the water bath and its contents were transferred to a large, insulating Styrofoam heat jacket to provide an average cooling rate of 4.15°C/hour. The contents were left to anneal slowly for a total period of 72 hours.

After this cool-down period, a 20µl aliquot of the solution was transferred to another microfuge tube and diluted with 10mM TAE Mg^{+2} buffer to give a final volume of 50µl and a final molarity of 1.6 pmol/µl. This solution was stored at 4°C until use.

A

Block A Blue:
G C A G | T C G C | A C G A | C C T G | G C G T ‖ C T G T | T G G C | T
T T T | G C C A | A C A G ‖ T T T G | T A C T | A C G C | A A T C | C T
G C ‖ C G T A | T C G A | C G =70

Block A Yellow:
C G T C | A G G C | T G C T | G T G G | T C G T ‖ G C =22

Block A Red:
C G C T | A C C G | T G C A | T C A T | G G A C ‖ T A A C | C A G T | G
C T C | G C T G | A T T T ‖ T T C A | G C G A | G T T A | C C G C | A T
C G ‖ G A C A | G C A G | C =69

Block A Cyan:
A G T A | C A A C | G C C A | C C G A | T G C G ‖ G T C A | C T G G | T
T A G | T G G A | T T G C ‖ G T =42

Block A Green:
G C C A | T C C G | T C G A | T A C G | G C A C ‖ C A T G | A T G C | A
C G =31

Block B Blue:
G A T G | G C G A | C A T C | C T G C | C G C T ‖ A T G A | T T A C | A
C A G | C C T G | A G C A ‖ T T G A | C A C =47

Block B Green:
G T A G | C G C C | G T T A | G T G G | A T G T | C =21

Block B Red:
C T G A | C G C T | G G T T | G C A T | C G G A | C G A T | A C T A | C
A T G | C C A G | T T G G ‖ A C T A | A C G G | =48

Block B Cyan:
T G T A | G T A T | C G T G | G C T G | T G T A ‖ A T C A | T A G
C | G G C A | C C A A | C T G G ‖ C A =42

Block B Yellow:
G A C T | G C G T | G T C A | A T G C | T C A C ‖ C G A T | G C A A | C
C A G | =32

B

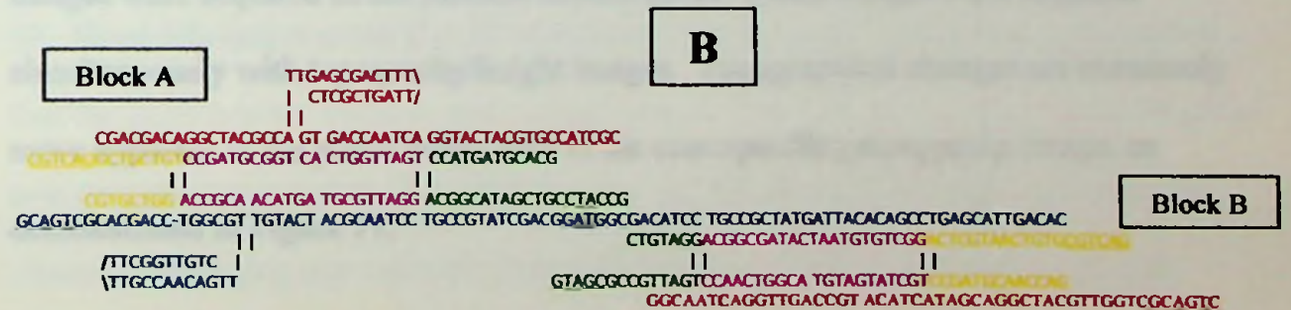

Figure 16: A) Sequence of oligonucleotides used in nanoarray preparation. All sequences are listed 5' to 3'. The number following each sequence is the number of bases included in the strand. B) Relative orientation of oligonucleotides listed in 11A.

AFM SAMPLE PREPARATION

Sample preparation included cutting a 0.5-inch square of mica from a Muscovite sheet (Alfa Aesar). This mica was mounted to the sample holder using double-sided carbon tape (Shinto Paint Company, Limited). A fresh, atomically flat, mica surface was exposed by peeling off the top layers with a strip of transparent tape. For sample I, two drops of the 1.6-pmol/μl solution were placed on this fresh surface using a disposable glass Pasteur pipette. After allowing this to dry for approximately 3 minutes, the surface was rinsed with 2 drops of distilled water. The sample holder was tilted to allow excess water to run off. Remaining water was allowed to dry at room temperature for 2 minutes. For sample II, another mica surface was prepared. Two drops of the 1.6 pmol/μl solution were applied and allowed to dry in the same manner as sample I. However, for sample II, the rinsing procedure of adding two drops distilled water and allowing to dry for two minutes was repeated a total of three times. When not in use, these samples were preserved in a glass dessicator (drierite loaded).

AFM IMAGING

All imaging was performed with a ThermoMicroscopes Autoprobe Research scanning probe microscope located at Union Carbide Corporation Technical Center. All images were acquired in intermittent contact mode. Phase images were acquired simultaneously with topography/height images. Topographical changes are commonly more apparent in the phase image than in the corresponding topography image, as demonstrated in Figure 17.

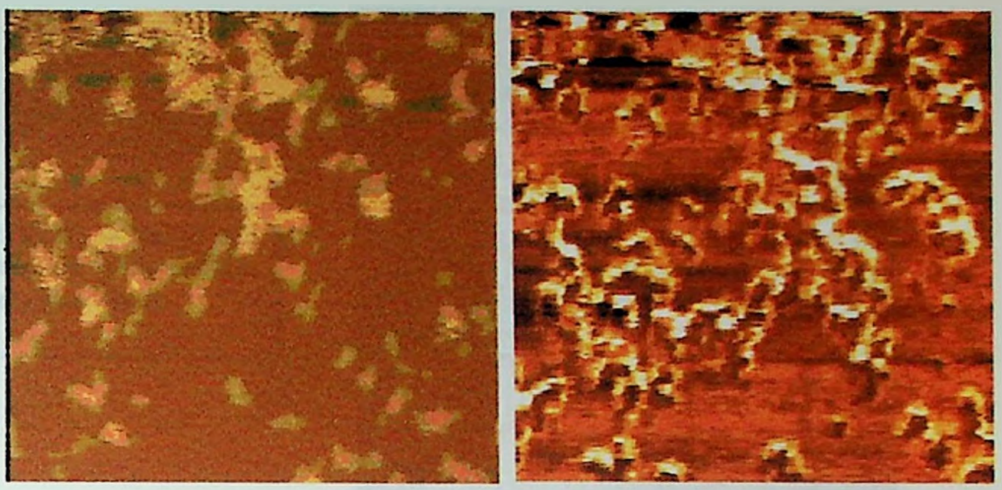

Figure 17: Topography (left) and phase (right) images of DNA fragments in air. Scan size was 1.00μm.

All images were acquired with V-shaped cantilevers, #ULCT-AUMT-AB, purchased from ThermoMicroscopes. The reported force constant was 0.26 N/m. Included images were acquired at a set-point amplitude ratio, $r_{sp}=A_{sp}/A_0$, near 0.8 where A_{sp} is the set-point amplitude, and A_0 is the amplitude of the free cantilever. Typical A_0 values ranged from 60-70 nanometers. Scan rates were typically 0.8 Hz (32).

RESULTS AND DISCUSSION

Imaging sample I began using a resonant frequency of about 300 kHz. A large white "carpet" seemed to cover an expansive area of the sample surface, as seen in Figure 18. Since this carpet could also be visualized with the optical scope, it was concluded that the layer was too thick to yield useful images. The film was assumed to be a layer of salt, precipitated out of the TAE buffer solution. Because this salt layer was such an obstacle in imaging any materials beneath it, it was agreed that the rinsing phase in sample preparation must be extended in order to minimize the presence of these salts.

Figure 18: Phase image of salt layer formed on mica surface. Scan range was 1.28μm.

A more thoroughly rinsed sample, Sample II was imaged using a resonance frequency of around 66 kHz. Using a scan rate of 0.8 Hz, the tip of an array was observed in one 8.0 μm x 8.0 μm scan. For closer examination the scan size was reduced to 3.271 μm, and the scan rate increased to 1.0Hz. The scanned image is presented in Figure 17. From this image, the array was determined to be more than 2 μm in length. Smaller scan sizes of 1.351 and 0.6080 μms were acquired. These images are presented in Figures 19 and 20, respectively.

Figure 19: Flattened phase image of tip of DNA nanoarray. The black dots surrounding the array are believed to be DNA fragments. Scan size 3.271 μm.

Figure 20: Phase image of 1.351μm view of DNA nanoarray seen in Figure 12.

Figure 21: Phase image of 0.6080μm view of nanoarray seen in Figure 14.

Striations visible on the surface of the crystal found in Figures 19 and 20 were attributed to DNA hairpins present in Building Block A, as shown in Figure 16. The separation between striations was determined to be 32 nm, see Figure 22. This is consistent with the findings reported by Winfree et al., (12), where striations were predicted by molecular modeling to be 32 nm apart and confirmed to be approximately 33nm apart. These striations were an integral part of identifying the DNA nanoarrays. They served as a unique identification tool in that only if the crystals formed as predicted would the hairpins have been arranged in a discernable, recognizable pattern. The images obtained in air are comparable in quality to those obtained in solution.

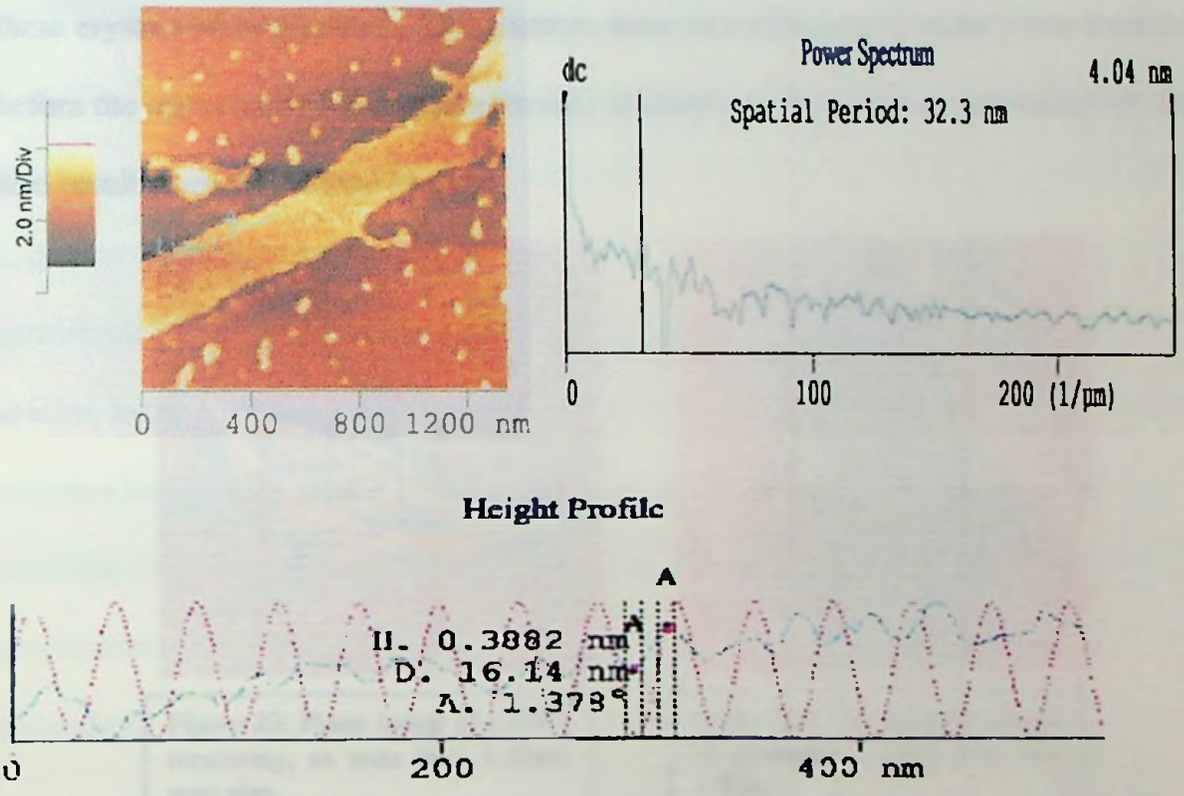

Figure 22: Pictured at left is a topography image of a nanoarray, flattened line-by-line. The figure on the right is the power spectrum resulting from the line scan indicated by the green line in the image. This indicates the distance between two subsequent striations (hairpins). Below is the height profile generated from the same line scan. The height o f the hairpin is 0.3882nm, and the distance measured between a high point (presumably a hairpin) and the low point is 16.14nm.

Two other objects were imaged under these conditions. The dimensions and structural characteristics of which were consistent with the presence of DNA nanoarrays. Figures 23 and 24 were imaged under conditions described above, with the exception that set point biases were –0.05450 μm and –0.06203μm for each. Humidity differences in the area as the day progressed may have required these changes in order to maintain a comparable resolution. Striations were observed in the arrays shown in Figures 23 and 24. Figure 23 displayed an irregular pattern of assembly. The irregular "holey" appearance of the array in Figure 24 could be due to degradation of the DNA by hydrolysis, since there was a large amount of water present in the TAE buffer in which these crystals were prepared. These arrays were stored for approximately two months before the opportunity for imaging became available. A high defect concentration could also result from malformed blocks.

Figure 23: Phase image of a DNA nanoarray, as seen in a 1.50μm scan size.

Figure 24: Topography image of nanoarray. Scan size was 5.00μm.

A slightly smaller value for the separation between striations than the reported 33nm was to be expected due to desolvation. Although arrays appear to be relatively unaffected by solvent evaporation, individual DNA fragments, which appeared around

each nanoarray imaged, are significantly affected by this process. The particulate, rounded appearance was the result of meniscus forces active during drying in air.

When imaged in a fluid cell, these fragments display the expected fiber (polymer) morphology. In fluid imaging, all materials present would be well solvated (12). DNA crystals were not subject to deformation upon drying in air due to adhesion to the mica surface and their added structural rigidity (33).

Imaging DNA in air has been widely studied. One of the proposed imaging condition modifications was based upon varying buffer pH and cation concentration. In a study by Thomson et al., emphasizing the importance of cation concentration on binding DNA to mica substrates, DNA was adhered to mica under of solution of pH of 7.5 and 2mM Zn^{+2}. These were the optimum parameters in the formation of a Zn^{+2} ion bridge between negatively charged DNA and the mica. The importance of solution composition is demonstrated by an experiment in which the solution was varied using a flow-through system yielding conditions in which Zn^{+2} precipitated out of solution and the DNA present became free-floating (34). In another study by M. J. Allen, dry nitrogen gas was released into a small plexiglass imaging chamber to maintain a constant, low relative humidity (35). For the method and samples described here, such changes in sample preparation, instrument accessory, or in imaging conditions were not found to be necessary.

CONCLUSIONS

Imaging DNA by scanning probe microscopy has been the goal of researchers since the introduction of the STM, scanning tunneling microscope, in 1982 (36). With

the advent of AFM, the insulating nature of DNA was no longer a barrier to be overcome. Imaging still proved troublesome, however, due to the flexibility of single and duplex strands of DNA. A strong binding affinity for mica held promise, but a limited number of anchoring sites within individual strands caused poor adhesion, and therefore poor imaging. In the circumstance of DNA objects, such as the two-dimensional nanoarrays described here, the number of anchoring sites is increased by several fold. This improved adhesion allows thorough examination of the much more rigid substrate. Through incorporation into the matrices of DNA objects, properties of the individual components can be evaluated with high-resolution imaging. The sample preparation and imaging parameters described here can be utilized to garner information valuable to both well-established and developing fields, such as nanotechnology.

SPECTROSCOPIC ANALYSIS OF DNA OBJECT SELF-ASSEMBLY

INTRODUCTION

It is postulated that one of the oligonucleotides contained within each block may be playing a role similar to that of a molecular chaperone. Molecular chaperones, also known as "helper proteins," are a class of proteins whose sole function is to aid in protein folding. Current theory holds that this is accomplished in most cases by binding to the target protein itself, thereby guiding folding, often by isolating possible binding sites that may take part in misfolding or aggregation, processes which compete with appropriate protein folding (37). These oligonucleotides, which incorporate into the final structure, differ from true molecular chaperones in that a molecular chaperone is no longer associated with its target molecule once folding or assembly is complete (38). The focus of this research was to determine the extent of this relationship within a single DNA block. This was investigated by studying the annealing process of the sequences shown in Figure 25. The red, cyan, and blue oligos were chosen for interrogation. The central loop structure is a motif common to all blocks. The predicted high annealing temperature of the red-cyan pair lead to the expectation that this pairing is the first step in the process of block self assembly. If an oligonucleotide is acting as a chaperone, there will be a shift in annealing temperature when the chaperone is present. For example, the temperature determined for the annealing of the cyan sequence to the blue should be raised when the red sequence is also present. The higher annealing temperature in the presence of the chaperone is indicative of a higher stability, i.e. stronger bonding as a result of chaperone binding induced conformational rigidity. The anticipated synergistic interactions are demonstrated schematically in Figure 26.

A

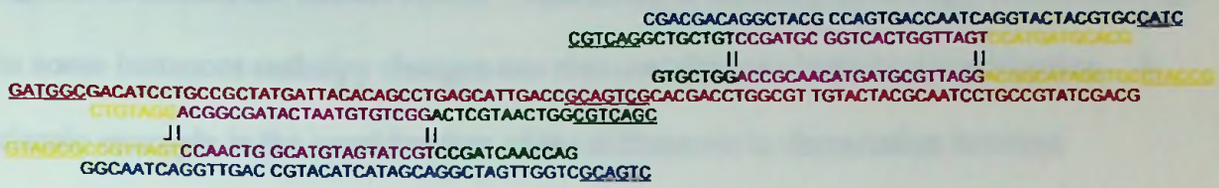

B

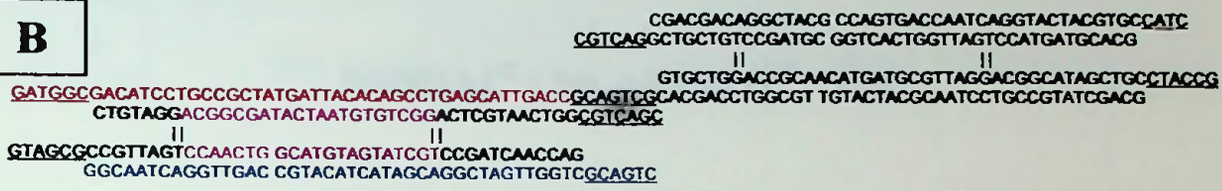

C

DAE-O AB Lattice A red:
GAT GGC GAC ATC CTG CCG CTA TGA TTA CAC AGC CTG AGC ATT GAC C

DAE-O AB Lattice A cyan:
GCA TGT AGT ATC GTG GCT GTG TAA TCA TAG CGG CAC CAA CTG

DAE-O AB Lattice A blue:
CTG ACG CTG GTT GAT CGG ACG ATA CTA CAT GCC AGT TGG ACT AAC GG

DAE-O AB Lattice A yellow:
GTA GCG CCG TTA GTG GAT GTC

DAE-O AB Lattice A green:
CGA CTG CGG TCA ATG CTC ACC GAT CAA CCA G

DAE-O AB Lattice B green:
CGT CAG GCT GCT GTG GTC GTG

DAE-O AB Lattice B yellow:
GCC ATC CGT CGA TAC GGC ACC ATG ATG CAC G

DAE-O AB Lattice B cyan:
GGT CAC TGG TTA GTG GAT TGC GTA GTA CAA CGC CAC CGA TGC

DAE-O AB Lattice B blue:
CGC TAC CGT GCA TCA TGG ACT AAC CAG TGA CCG CAT CGG ACA GCA GC

DAE-O AB Lattice B red:
GCA GTC GCA CGA CCT GGC GTT GTA CTA CGC AAT CCT GCC GTA TCG ACG

Figure 25: **A)** DAE Blocks A and B. **B)** Block A red, cyan, and blue were used in spectroscopic studies to determine annealing temperatures. **C)** Listing of sequences used in this work.

The rigid tethering of binding sites giving exceptional stability to multidentate ligands is termed the chelate effect. This effect is basically an entropy effect, although in some instances enthalpy changes can also contribute to improved stabilization. A classic example is the consideration of the differences in dissociation between ethylenediamine complexes and ammonia complexes as in the following reaction:

$$[Ni(NH_3)_6]^{+2} + 3en \rightarrow [Ni(en)_3]^{+2} + 6NH_3$$

If an ammonia molecule dissociates from the complex and is carried off into solution, the probability of it returning to the complex is unlikely. Conversely, if one of the amine groups of the ethylenediamine dissociates from the complex, it is retained by the end still attached to the nickel. The nitrogen atom can move only a minute distance and can easily reach a conformation in which it can reattach to the nickel. The complex, $[Ni(en)_3]^{+2}$, has a much smaller probability of dissociating and is found to be more stable (39). The conformation of the central loop structure studied in Block A is believed to have a similar relationship. As seen in Figure 26, the Blue sequence attaches to the central bidentate Red-Cyan complex. Without the anchoring effect of the Red chaperone sequence, the probability of the Cyan binding sites finding the correct orientation for binding to the Blue sequence would be low.

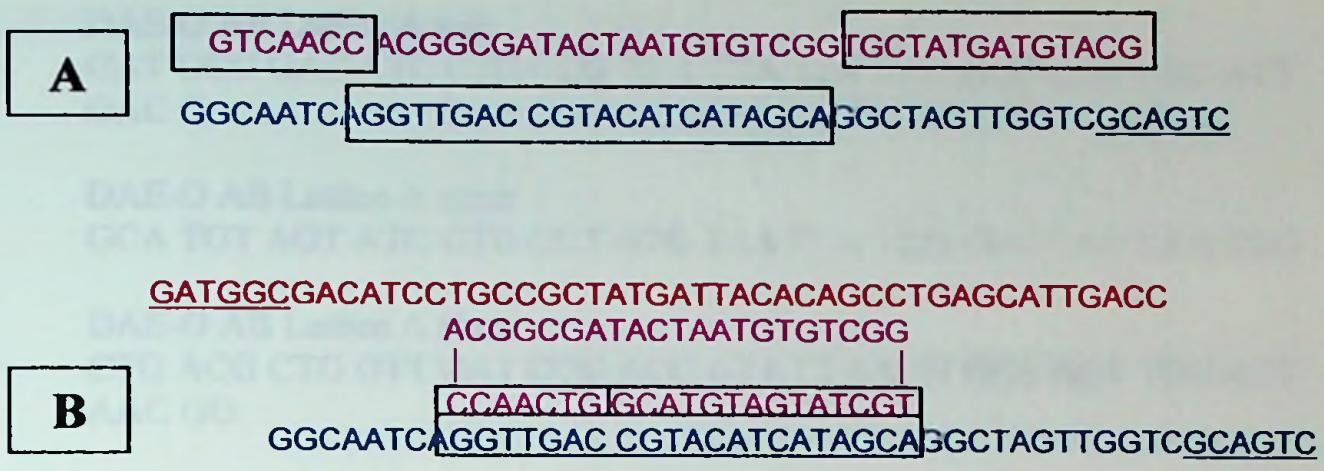

Figure 26: A) Binding site geometry without chaperone. Boxed areas indicate target binding sites. B) Chaperone-oriented binding site geometry.

PRELIMINARY ESTIMATES OF ANNEALING TEMPERATURES

All sequences were assessed before spectroscopic study using OLIGO 4.0 Primer Analysis Software (Molecular Biology Insights, Inc.), a software program developed for calculating and reporting oligonucleotide properties. OLIGO evaluates DNA sequences by the three methods described above, the nearest neighbor method, the %GC method and the Wallace Rule (19). The red, cyan and blue sequences of Block A were evaluated to determine annealing temperature of both the complete sequence and of the prospective binding sites within each strand. These results are summarized in Figure 27 and Table 1.

DAE-O AB Lattice A red:
GAT GGC GAC ATC CTG CCG CTA TGA TTA CAC AGC CTG AGC ATT GAC C

DAE-O AB Lattice A cyan:
GCA TGT AGT ATC GTG GCT GTG TAA TCA TAG CGG CAC CAA CTG

DAE-O AB Lattice A blue:
CTG ACG CTG GTT GAT CGG ACG ATA CTA CAT GCC AGT TGG ACT AAC GG

GATGGCGACATCC-TGCCGCT-ATGATTACACAGCC-TGAGCATTGACC

[Section 1 13 bases] [Section 2 21 bases] [Section 3 12 bases]

ACGGCGA-TACTAATGTGTCGG [section 4, 21 bases]
| |
CCAACTG GCATGTAGTATCGT
[Section 5, [section 6, 14 bases]
7 bases]

GGCAATCA-GGTTGAC-CGTACATCATAGCA-GGCTAGTTGGTCGCAGTC

[Section 7, [Section 8, [Section 9, 14 bases] [Section 10, 18 bases]
8 bases] 7 bases]

Figure 27: Sequences used in OLIGO analysis.

Sequence	# Bases	Td (Nearest Neighbor Method)	Tm (%GC Method)	Tm (Wallace Rule)
Block A Red	46	95.2	89.1	142.0
Block A Cyan	42	88.9	85.9	126.0
Block A Blue	47	93.4	88.9	144.0
Sequence 1	13	44.6	54.8	42
Sequence 2	21	67.8	70.8	64
Sequence 3	12	32.1	45.8	36
Sequence 4	21	67.8	70.8	64
Sequence 5	7	-16.1	8.5	22
Sequence 6	14	33.8	50.9	40
Sequence 7	8	-0.8	17.6	24
Sequence 8	7	-18.1	2.6	20
Sequence 9	14	38.8	53.8	42
Sequence10	18	61.7	66.8	56
Sequences 5+6	21	61.9	68.9	62
Sequences 8+9	21	62.6	68.9	62

Table 1: OLIGO results for sequences defined in Figure 27.

The predicted high annealing temperature listed here for Section 2, the binding site for the red oligo, and its conjugate, section 4 of the cyan strand, lead to the

expectation that this pair would anneal first during two-dimensional nanoarray assembly, and hence serve as the chaperone during the remainder of the annealing process.

MATERIALS AND METHODS

All oligonucleotides used in this phase of the study were acquired from the Marshall University DNA Core Facility, where they were synthesized using an ABI 394 DNA/RNA Synthesizer by standard methods. Finished oligos are contained in 1.5ml microfuge tubes. The actual yield of each oligo was 35.574nmol for Red, 49.132nmol for Cyan and 33.522nmol for Blue (Refer to Appendix B). Ten microliters of 10mM Mg^{+2} TAE buffer, described previously, were added to each microfuge tube to hydrate the DNA, giving final concentrations of 3.5574nmol/µl, 4.9132nmol/µl, and 3.3522nmol/µl for Red, Cyan and Blue sequences, respectively.

UV-VISIBLE SPECTROPHOTOMETRY

Samples for study by UV-visible spectrophotometry were prepared in a standard screw-cap quartz cuvette with a 1cm light path. In each instance, 3.0ml of TAE buffer were placed in the cuvette using a calibrated plastic disposable pipette. A blank spectrum was taken of this buffer and cuvette using the HP 8452A spectrophotometer. To this system, 5.0µl each of Block A Red and Block A Cyan were added. The screw cap was securely placed on the cuvette and it was sealed using parafilm to prevent evaporation. The cuvette was placed in the spectrometer sample chamber when the temperature bath reading was 55°C. The room temperature was noted. The cuvette remained in the

sample chamber until the temperature reached and maintained a temperature of 95.0°C for 5 minutes. At this time a time-based scan was begun. Spectra were taken over the range of 200 to 300nm with an integration time of 0.5s every 5 minutes for 9 hours. Immediately after initiating the scan the temperature bath setting was reduced to a target temperature of 20.0°C. The refrigeration was disabled to allow for slower annealing. At the conclusion of the scan, each sample spectrum was analyzed to ascertain the absorbance value at 260nm. The cuvette remained in the sample chamber during this period, while the temperature bath was resetting to 95.0°C. At 95.0°C, 0.5µl of Block A Blue were added to the cuvette. The cap was replaced and again sealed with parafilm. The contents of the cuvette were allowed to equilibrate at 95.0°C for 5 minutes. The time-based scan was repeated with the same parameters as described above. Single wavelength analysis at 260nm was performed on the resulting spectra. This method was repeated for samples containing Block A Blue +Block A Cyan and Block A Blue + Block A Cyan + Block A Red.

SPECTROFLUOROMETRY

A solution of SYBR Green I nucleic acid stain was prepared by adding 0.5µl SYBR Green I 10,000X concentrate in DMSO (Molecular Probes, Inc.) to 10.0ml TAE buffer to give a 0.05µl/ml working solution. Samples for study by spectrofluorometry were prepared in standard screw-cap quartz cuvettes with 1cm light paths. Three milliliters of 0.05µl/ml SYBR Green I solution were added to each cuvette. To Cuvette I, 5.0µl each of Block A Blue and Block A Cyan were added. The screw cap was replaced and the cuvette was sealed with parafilm. Cuvette I was placed in position 1 of

the sample changer within the sample chamber of the SPEX Fluorolog III fluorimeter. Cuvette II contained 5.0µl each of Block A Red and Block A Cyan. This cuvette was placed in position 2 of the sample changer. The excitation and emission wavelengths were determined using standard methods and found to be 493nm for maximum excitation and 523nm for maximum emission. The temperature bath was set for 95.0°C. After an equilibration period of 5 minutes, a constant wavelength scan was initiated. Parameters included the default setting to keep shutters closed except during measurements, the mentioned excitation and emission wavelengths, as well as a starting temperature of 95.0°C, an ending temperature of 20.0°C, and instructions to collect data at 46 temperatures in between these values. A low tolerance value was assigned, ±0.2°C, and an equilibrium time of 1.0 minute at each temperature before taking spectra was set. The sample changer rotates to allow data for Cuvette II to be taken immediately following data collection for Cuvette I. This gives the added benefit of studying both samples in an identical environment.

At the conclusion of this temperature-based scan, the temperature bath was reset to 95.0°C. When the target temperature was attained, 5.0µl Block A Red were added to Cuvette I and 5.0µl Block A Blue were added to Cuvette II. Both cuvettes were resealed with parafilm and returned to their respective positions within the sample changer. A constant wavelength scan was repeated with the same parameters as above.

RESULTS AND DISCUSSION

The raw data obtained from the preceding methods was utilized in the construction of plots of absorbance vs. temperature and intensity vs. temperature.

Representative plots may be seen below in Figures 28 and 30. Notice in Figure 28 that the trace of Red + Cyan is more intense than that of Red + Cyan + Blue. Logically, an increase by 50% in intensity is predicted due to the addition of material that should produce 50% more duplex bases of DNA. The observed decrease in intensity is attributed to a phenomenon known as concentration quenching (26). In these duplex oligonucleotides, the intercalated fluorescent dye molecules are already in close contact. When the third oligonucleotide is added, the rigid conformation of the nanoarray pulls the oligonucleotide-dye complexes into close proximity. This closeness or contact of neighboring complexes may produce quenching through energy transfer. This quenching results in a lowered observed intensity. This supposition was tested by studying a system comprised of two similar sets of complimentary strands, which do not interact to form block structures. The complimentary sets of oligonucleotides studied were the Red + Cyan sequences of Block A and the Red + Cyan sequences of Block B. As seen in Figure 25, the Red + cyan sequences of Block B correspond in position to Blue + Cyan of Block A. The inability of Block B Red+ Cyan to form a duplex with Block A Red + Cyan provides the basis for this control experiment. The results are plotted in Figure 29. The resultant intensity-temperature curve, although not displaying the ideal factor of 2 gain in intensity, does show increased fluorescence relative to the independent pairs. This experimental result supports the hypothesis that the double helix proximity required by the double-crossover structure leads to quenching.

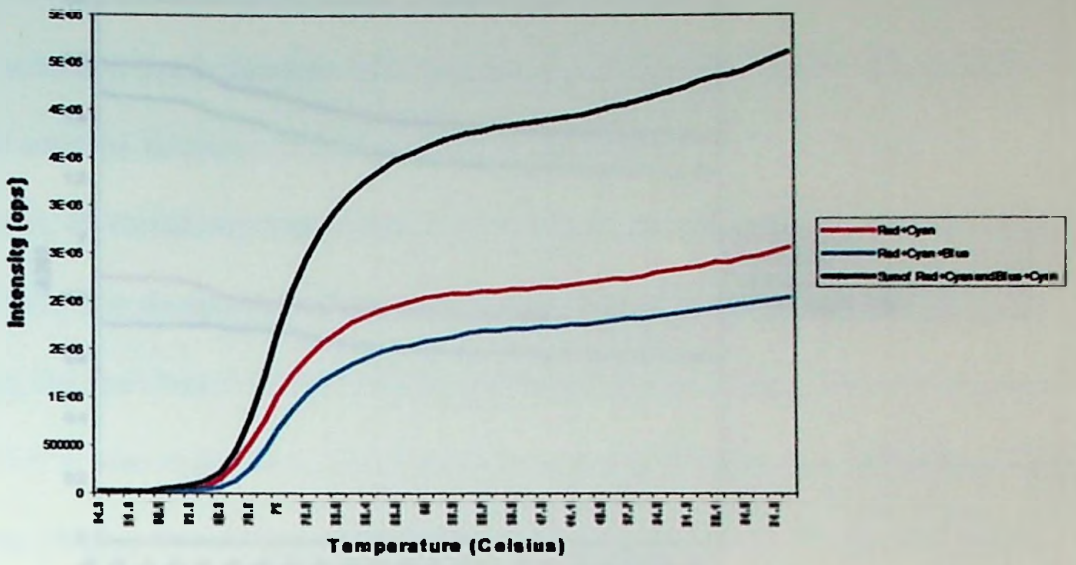

Figure 28: Fluorescence plot of Red + Cyan, Red + Cyan + Blue, and Sum of Red + Cyan and Blue + Cyan.

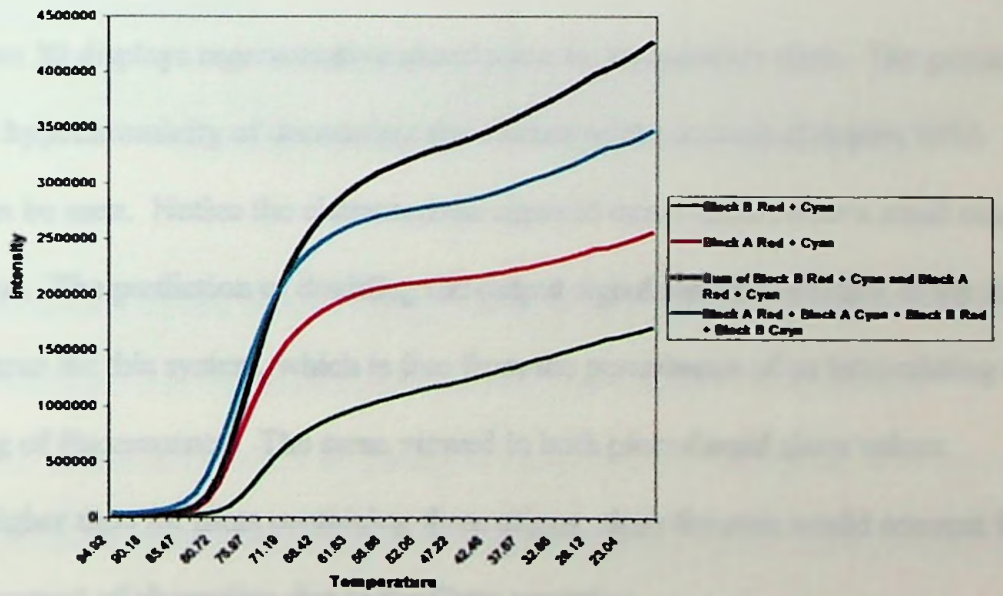

Figure 29: Fluorescence intensity vs. temperature plot of Block B Red + Cyan, Block A Red + Cyan, the numerical sum of Block B Red + Cyan and Block A Red + Cyan and Block A Red + Block A Cyan + Block B Red + Block B Cyan.

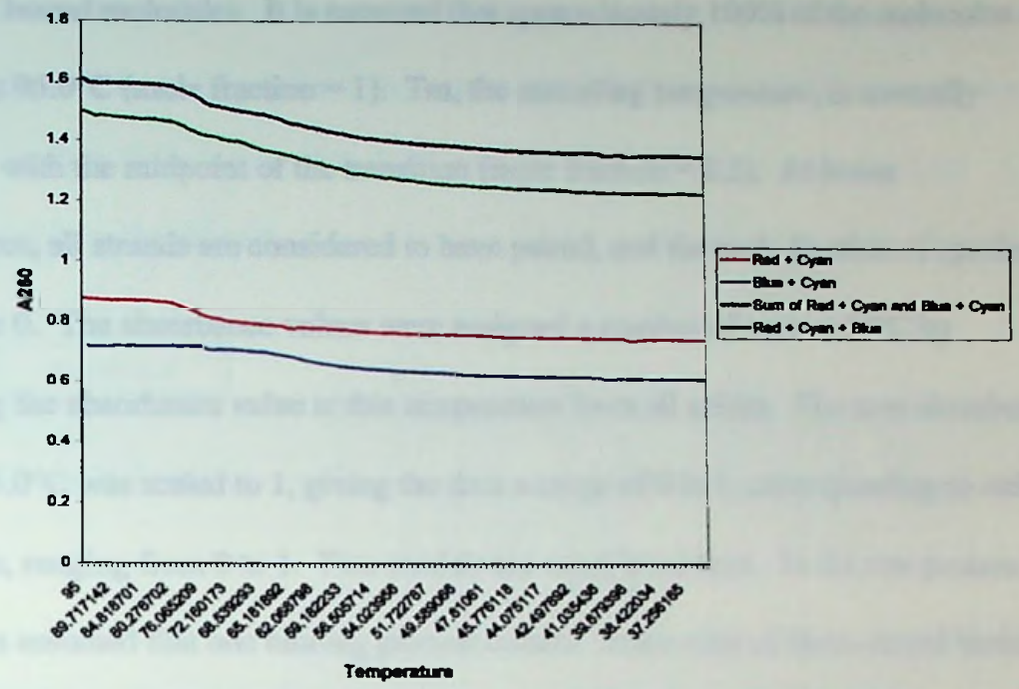

Figure 30: Plot of absorbance at 260nm vs. temperature for Red + Cyan, Red + Cyan + Blue, and Numerical Sum of Red + Cyan and Blue + Cyan.

Figure 30 displays representative absorbance vs. temperature plots. The general trend due to hypochromicity of decreasing absorbance as the amount of duplex DNA increases can be seen. Notice the characteristic sigmoid curve occurs over a small range of absorbance. The prediction of doubling the output signal with the addition of the third oligo holds true for this system, which is free from the perturbance of an intercalating dye or quenching of fluorescence. The sums viewed in both plots should show values somewhat higher than for plots containing three oligos, since the sum would account for double the amount of absorption due to the Cyan sequence.

SPECTROSCOPIC DATA ANALYSIS

The data shown in the preceding section had to be normalized in order to extract binding parameters. Both fluorescence and absorbance variations reflect changes in the

fraction of bound molecules. It is assumed that approximately 100% of the molecules are unpaired at 95.0°C (mole fraction = 1). Tm, the annealing temperature, is normally associated with the midpoint of the transition (mole fraction = 0.5). At lower temperatures, all strands are considered to have paired, and the mole fraction of species unpaired is 0. The absorbance values were assigned a number of zero at 50°C by subtracting the absorbance value at this temperature from all points. The new absorbance value at 95.0°C was scaled to 1, giving the data a range of 0 to 1, corresponding to order parameters, ranging from 0 to 1. Two models are considered here. In the one process model, it is assumed that one binding process occurs. In the case of three-strand binding, the characteristic temperature (Tm) associated with this process can be compared to the temperatures determined for the pairs involved. A raised average Tm could be used to indicate positive cooperativity.

$$F(T, \Delta H, Tm) := \left[\frac{e^{\left[\frac{\Delta H}{R}\cdot\left(\frac{1}{Tm}-\frac{1}{T}\right)\right]}}{1+\left[e^{\frac{\Delta H}{R}\cdot\left(\frac{1}{Tm}-\frac{1}{T}\right)}\right]} \right] \quad (40)$$

Equation 5

In the second model, the annealing curve is modeled as reflecting two separable binding events with different characteristic binding temperatures and associated enthalpies. In the second model a weighing factor, a, is used to determine the relative contribution of each process to the observed annealing event. The weighing factor could be represented as an indicator of the influence of the primary binding event on the secondary event.

These normalized plots were fit to a function by a non-linear least squares regression using Mathcad 8 to determine precise values for annealing temperatures and

thermodynamic data. The function to which data was fit is a form of the van't Hoff equation; please refer to Appendix D for a more detailed discussion. Single component systems were fit to Equation 5, while those systems believed to be two component systems were fit to Equation 6.

Equation 6

$$F(T, a, \Delta H, Tm) := (1 - a_1)\cdot\left[\frac{e^{\left[\frac{\Delta H_1}{R}\cdot\left(\frac{1}{Tm_1}-\frac{1}{T}\right)\right]}}{1+\left[e^{\left[\frac{\Delta H_1}{R}\cdot\left(\frac{1}{Tm_1}-\frac{1}{T}\right)\right]}\right]}\right] + a_1\cdot\frac{e^{\left[\frac{\Delta H_2}{R}\cdot\left(\frac{1}{Tm_2}-\frac{1}{T}\right)\right]}}{1+\left[e^{\left[\frac{\Delta H_2}{R}\cdot\left(\frac{1}{Tm_2}-\frac{1}{T}\right)\right]}\right]}$$

T is the temperature at which a data point was collected (see Appendix C); **a** is a weighing factor, to be discussed below; **ΔH** is the reaction enthalpy; **Tm** is the annealing temperature; and **R** is the gas constant, 8.314 J/K*mol. The results obtained from all fits are shown graphically in Figures 31 – 40 and summarized in Table 2.

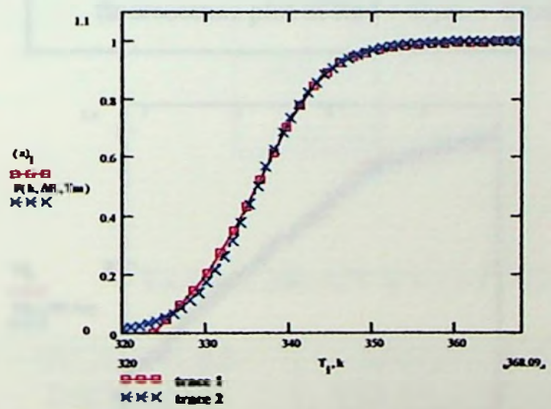

Figure 31: A single-process model fit of fluorescence plot of Blue + Cyan.

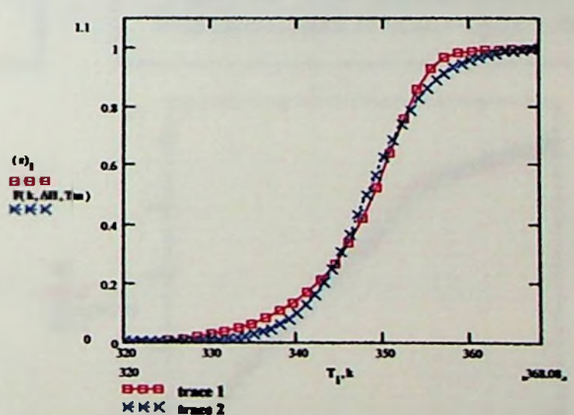

Figure 32: A single-process model fit of fluorescence plot of Red + Cyan.

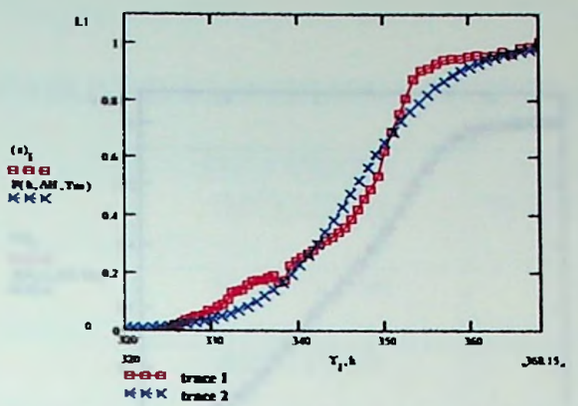

Figure 33: A single-process model fit of UV plot of Red + Cyan.

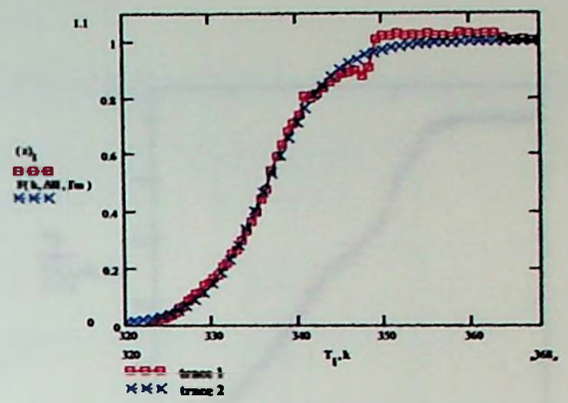

Figure 34: A single-process model fit of UV plot of Blue + Cyan.

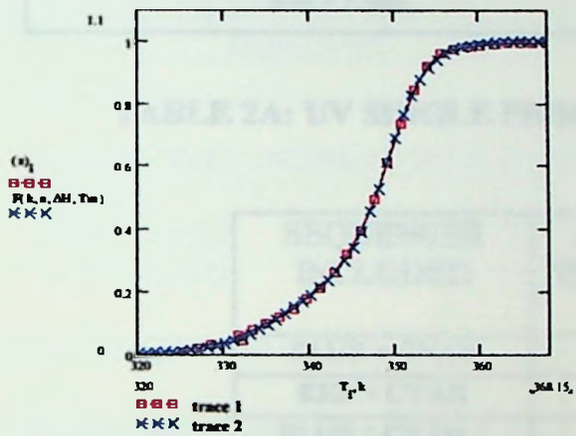

Figure 35: A two-process model fit of fluorescence plot of Red + Cyan + Blue.

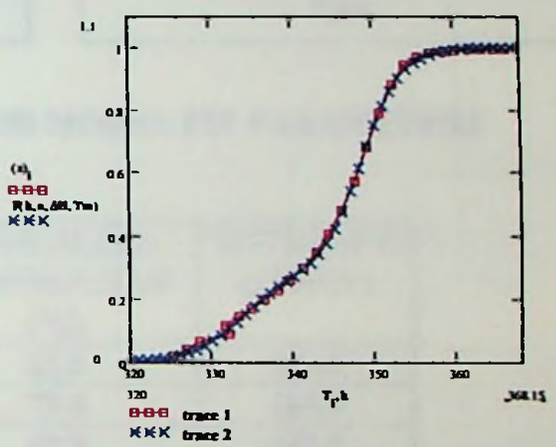

Figure 36: A two-process model fit of fluorescence plot of Blue + Cyan + Red.

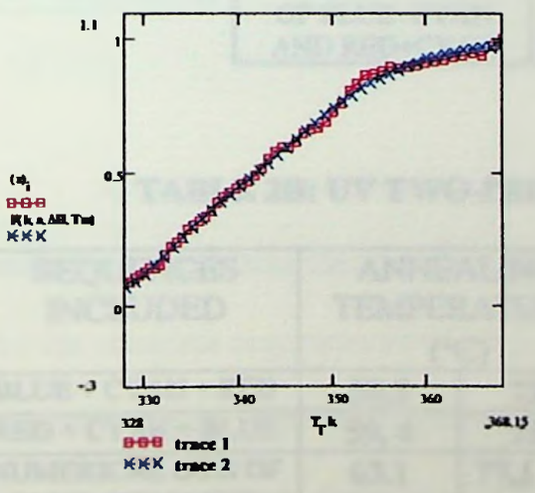

Figure 37: A two-process model fit of UV plot of Red + Cyan + Blue.

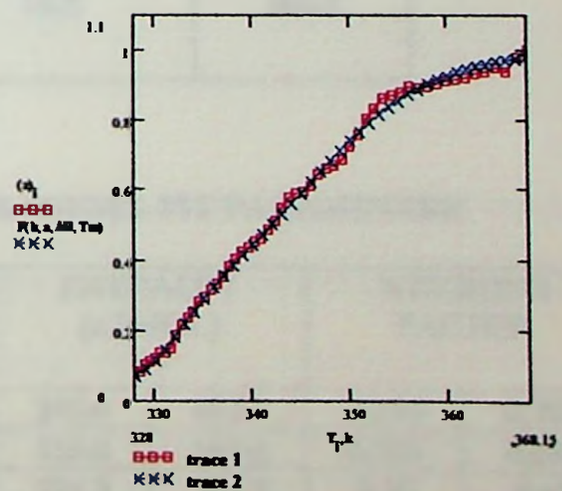

Figure 38: A two-process model fit of UV plot of Blue + Cyan + Red.

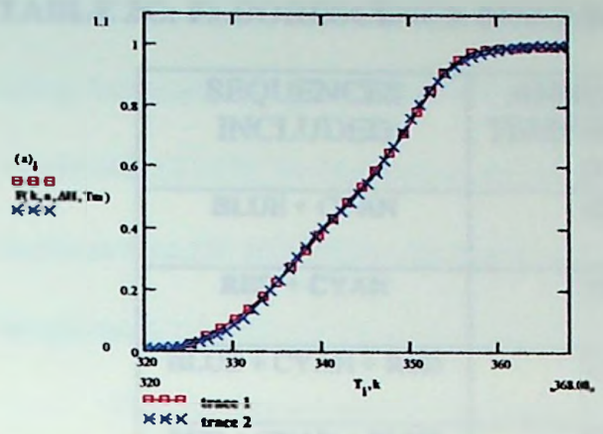

Figure 39: A two-process model fit of fluorescence plot of the Sum of Blue + Cyan and Red + Cyan.

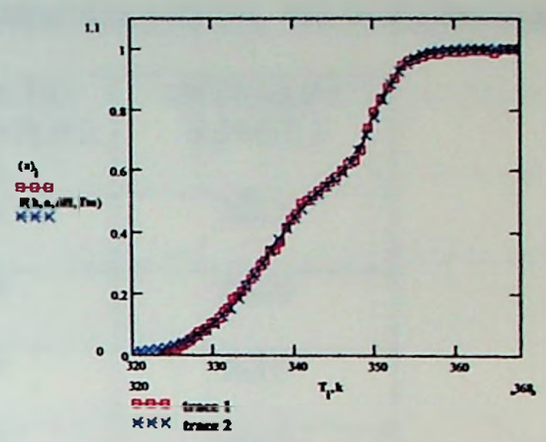

Figure 40: A two-process model fit of UV plot of the Sum of Blue + Cyan and Red + Cyan.

TABLE 2A: UV SINGLE PROCESS MODEL FIT PARAMETERS

SEQUENCES INCLUDED	ANNEALING TEMPERATURE (°C)	ENTHALPY (KJ/MOL)
BLUE + CYAN	63.3	249.6
RED + CYAN	73.4	183.6
BLUE + CYAN + RED	68.9	142.5
RED + CYAN + BLUE	70.3	152.6
NUMERICAL SUM OF BLUE+CYAN AND RED+CYAN	68.5	166.2

TABLE 2B: UV TWO-PROCESS MODEL FIT PARAMETERS

SEQUENCES INCLUDED	ANNEALING TEMPERATURE (°C)		ENTHALPY (KJ/MOL)		WEIGHING FACTOR	
BLUE + CYAN + RED	59.5	73.6	346.4	167.1	0.295	0.705
RED + CYAN + BLUE	59. 4	73.7	325.8	167.0	0.306	0.694
NUMERICAL SUM OF BLUE+CYAN AND RED+CYAN	63.1	77.1	594.3	241.2	0.38	0.62

TABLE 2C: FLUORESCENCE SINGLE-PROCESS MODEL FIT PARAMETERS

SEQUENCES INCLUDED	ANNEALING TEMPERATURE (°C)	ENTHALPY (KJ/MOL)
BLUE + CYAN	62.8	252.5
RED + CYAN	74.9	270.1
BLUE + CYAN + RED	71.7	208.9
RED + CYAN + BLUE	73.6	256.9
NUMERICAL SUM OF BLUE+CYAN AND RED+CYAN	66.6	177.0

TABLE 2D:FLUORESCENCE TWO-PROCESS MODEL FIT PARAMETERS

SEQUENCES INCLUDED	ANNEALING TEMPERATURE (°C)		ENTHALPY (KJ/MOL)		WEIGHING FACTOR	
BLUE + CYAN + RED	75.2	60.6	406.6	290.0	0.71	0.29
RED + CYAN + BLUE	76.0	64.5	440.2	240.0	0.721	0.279
NUMERICAL SUM OF BLUE+CYAN AND RED+CYAN	76.3	62.3	359.1	265.7	0.505	0.495

A comparison can be made between the calculated theoretical Tm values and the values extracted from these experimental results. The predicted annealing temperatures for the complete sequences of Block A Red, Cyan and Blue were much higher than the observed values. This was to be expected since only partial sequences were involved in the processes studied. Estimates for Sequences 2 and 4 listed in Table 1 fell short of the observed values for the annealing temperature of Red + Cyan by a significant margin.

Comparison of observed values for Blue + Cyan were much higher than predicted for the individual components, sections 5, 6, 8, and 9 but were fairly accurate for the predictions using the nearest neighbor method and the Wallace Rule considering sections 5 and 6 as a single unit (61.9°C by the nearest neighbor method and 62°C by the Wallace rule) and sections 8 and 9 (62.6°C by the nearest neighbor method and 62°C by the Wallace rule) as one unit.

The two-component fit lead to a "deconvolution" of the observed annealing temperature. Although fitting to a single-component model does give reasonable results, the improved fit of the two-process model indicates that this is a better description of the behavior of the system. This improvement of fit quality is clearly seen in Figure 41. The physical meaning of the fit parameters can now be considered.

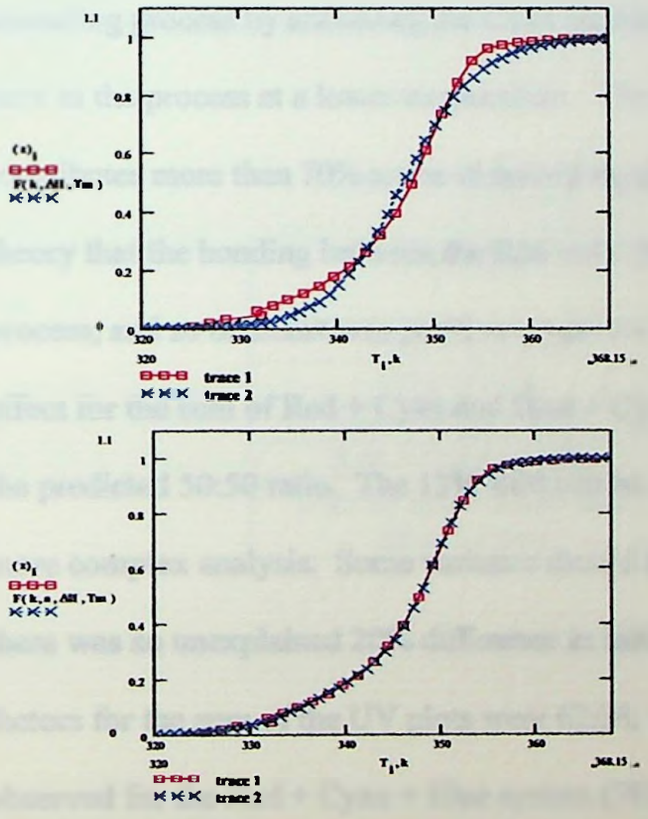

Figure 41: At top is the Red + Cyan + Blue Fluorescence Plot fit to Equation 5, a single-process fit. Shown below is the same plot fit to Equation 6,a two-process fit.

The weighing factor, a, was a crucial factor in fitting this data. This is evident in the results listed in Table 2. For example, looking again at the fluorescence plot of Red + Cyan + Blue, notice that annealing temperature derived from the single-process fit of the sum of Red + Cyan and Blue + Cyan, 66.6°C, is not merely an average of the two values derived from the two-process fit, 76.0°C and 64.5°C. If the two temperatures were evenly weighted, it would appear that the two binding sites, Red + Cyan and Blue + Cyan, were binding simultaneously and with equal precision, as in the case of the numerical sum of Red + Cyan and Blue + Cyan, where the weighing factors for the two annealing temperatures are virtually 50% for each component. The same is true for the two-process fit of Blue + Cyan + Red, where the resulting temperatures are 75.2°C and 60.6°C. According to the data, Red + Cyan must be binding first, driving the rest of the annealing process by anchoring the Cyan segment, so that the Blue segment may anneal later in the process at a lower temperature. The fact that the higher temperature process contributes more than 70% to the observed annealing curve further corroborates the theory that the bonding between the Red and Cyan binding sites dominate this annealing process, and so demonstrates positive cooperativity. There is some variance from this effect for the sum of Red + Cyan and Blue + Cyan in the UV plots. The weights are not the predicted 50:50 ratio. The 13% shift can be considered significant and may require more complex analysis. Some variance should have been anticipated however, since there was an unexplained 20% difference in initial absorbance values. The weighing factors for the sum of the UV plots were 62:38, while higher weighing factors were observed for the Red + Cyan + Blue system (70:30), again indicating, although weakly, cooperative phenomena.

CALCULATION OF ENTROPY CHANGES FROM EXPERIMENTAL VALUES

Consider the relation,

$$\Delta G = \Delta H - T \times \Delta S. \qquad \text{Equation 7}$$

The Gibbs free energy, ΔG, is equal to zero when $T = Tm$. Following rearrangement, Equation 7 becomes

$$\Delta S = -\Delta H / Tm. \qquad \text{Equation 8}$$

This equation was used to calculate entropy values for each of the annealing processes studied. Values for systems fit to the two-process model were determined by first calculating independent values using $\Delta S_1 = -\Delta H_1 / Tm_1$ and $\Delta S_2 = \Delta H_2 / Tm_2$, multiplying the resultant by the appropriate weighing factor, **a**, then adding ΔS_1 and ΔS_2. These results are summarized in Table 3.

Table 3A: Entropy Values for UV Curves

Sequences	ΔS J/K*mol
Blue + Cyan	-741.791
Red + Cyan	-529.736
Blue + Cyan + Red	-646.929
Red + Cyan + Blue	-633.965
Sum of Red + Cyan and Blue + Cyan	-1099

Table 3B: Entropy Value for Fluorescence Curves

Sequences	ΔS J/K*mol
Blue + Cyan	-751.584
Red + Cyan	-776.022
Blue + Cyan + Red	-1081
Red + Cyan + Blue	-1107
Sum of Red + Cyan and Blue + Cyan	-910.956

Because calculated entropy values for data from the two methods did not correlate, strong conclusions could not be drawn from these calculations.

CONCLUSION

Neither complimentarity nor the typical double-stranded DNA annealing process alone is sufficient in describing the processes involved in two-dimensional DNA nanoarray self-assembly. Although both contribute significantly, when multiple components are present, the system is more complex than for the case of annealing two oligonucleotide sequences. As shown here, the assembly and annealing behavior of only two oligonucleotides can be accurately predicted, but conventional models fall short when a third oligonucleotide is also considered. Positive cooperativity between oligonucleotides has been demonstrated through the presented two-process annealing models. An interpretation of the extracted weighing parameters is that, as postulated, the addition of the Red sequence to the Blue + Cyan system increases the temperature at which the majority of strands anneal. The same effect was observed for the addition of Blue to Red + Cyan. Experimental results confirm the assignment of the Red sequence as chaperone. The subsequent Red-Cyan complex acts as a bidentate ligand whose target binding sites are incorporated into the Blue sequence. The correlation of observed annealing temperatures for Blue + Cyan with those predicted for corresponding complimentary sections of the Blue and Cyan sequences lead to the assumption that annealing is occurring at these sites. The increase in high temperature melting fraction observed in the presence of the Red sequence is attributed to the cooperative effect.

APPENDIX A: DNA STRUCTURE

DNA is composed of a long chain of deoxyribonucleotides. Deoxyribonucleotides are composed of a sugar, a nitrogenous base, and one or more phosphate groups. The sugar found in DNA is 2-deoxy-β-D-furanose, commonly called 2'-deoxyribose. The structure of deoxyribose can be seen in Figure A.

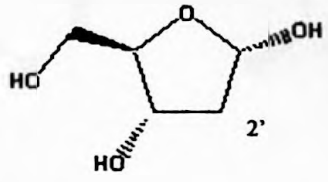

Figure A: Structure of 2'-deoxyribose, so called because of the absence of a hydroxyl group at the 2' position.

DNA also contains many phosphate groups, as in Figure B. It is this phosphodiester linkage that forms an integral part of the backbone of the DNA chain.

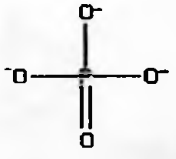

Figure B: Phosphate group

The nitrogenous bases can be one of two forms: purine or pyrimidine:

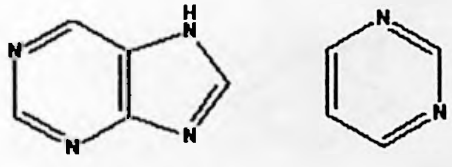

Figure C: DNA bases are derivatives of either purine (left) ar pyrimidine (right).

In DNA, there are two purine bases, Adenine (A) and Guanine (G), as seen in Figure D. There are two pyrimidine bases, Thymine (T) and Cytosine (C), shown in Figure E.

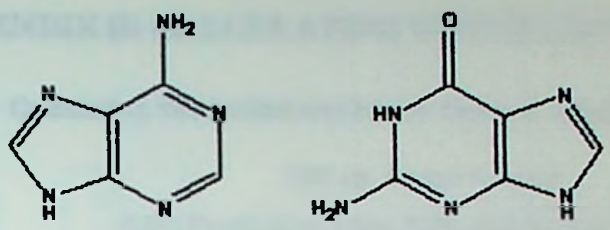

Figure D: Purine bases, adenine and guanine

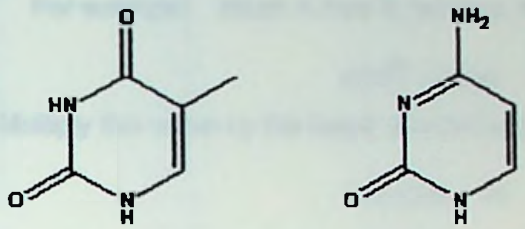

Figure E: Pyrimidine bases, thymine and cytosine

The bases are not incorporated into the chain itself, but are attached laterally through deoxyribose. This placement allows for interaction with other bases. This is how the bases form the rungs of the now famous DNA ladder.

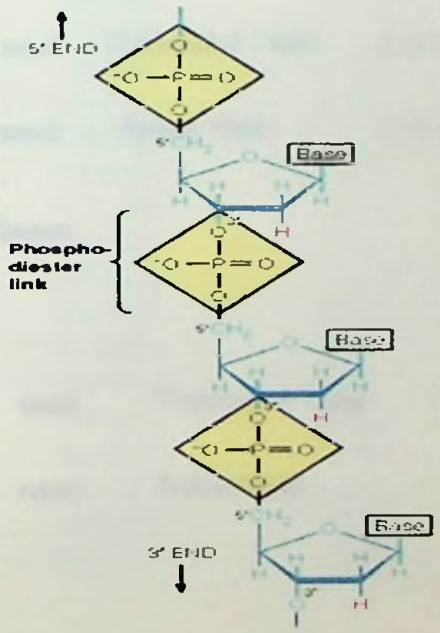

Figure F: Linkage of DNA components: phosphate group, deoxyribose and laterally positioned bases.

APPENDIX B: CALCULATING SYNTHETIC DNA YIELDS (41)

Calculating Theoretical and Actual Yields in Oligonucleotide Synthesis

200 nm Target Amount

OPC Purification gives 98% yield for each comprising oligonucleotide.

For example: Block A Red Sequence, 46 bases

$0.98^{46} = 0.395$

Multiply this value by the target amount to get the calculated yield in nM.

$0.395 \cdot 200 = 79$

Multiply the calculated nearest neighbor extinction coefficient by the meaured OD value to obtain the actual yield.

$\frac{\text{nmol}}{\text{A260}} \cdot \text{A260} = \text{nmol}$ $2.31 \cdot 15.4 = 35.574$

Block A Red, 46 bases

$0.98^{46} = 0.395$

$0.395 \cdot 200 = 79$ nmol Theoretical Yield

$2.31 \cdot 15.4 = 35.574$ nmol Actual Yield

Block A Blue, 47 bases

$0.98^{47} = 0.387$

$0.387 \cdot 200 = 77.4$ nmol Theoretical Yield

$2.22 \cdot 15.1 = 33.522$ nmol Actual Yield

Block A Cyan, 42 bases

$0.98^{42} = 0.428$

$0.428 \cdot 200 = 85.6$ nmol Theoretical Yield

$3.46 \cdot 14.2 = 49.132$ nmol Actual Yield

APPENDIX C: RAW SPECTROSCOPIC DATA

Fluorescence Data for Blue + Cyan, Red + Cyan, and Numerical Sum

Temp °C	Blue + Cyan	Temp °C	Red + Cyan	Temp °C	Sum of Red + Cyan and Blue + Cyan
94.94	6172	94.94	14324	94.94	20496
93.34	5981	93.34	12958	93.34	18939
91.77	6337	91.77	14469	91.77	20806
90.2	7532	90.2	17771	90.2	25303
88.63	9148	88.63	22582	88.63	31730
87.06	11447	87.06	30568	87.06	42015
85.47	14737	85.47	44295	85.47	59032
83.89	18399	83.89	75536	83.89	93935
82.31	23369	82.31	151697	82.31	175066
80.73	31057	80.73	303163	80.73	334220
79.15	40905	79.15	519653	79.15	560558
77.56	53860	77.56	768814	77.56	822674
75.97	70511	75.97	1014703	75.97	1085214
74.38	95278	74.38	1235883	74.38	1331161
72.78	129459	72.78	1419738	72.78	1549197
71.2	182901	71.2	1571150	71.2	1754051
69.6	259289	69.6	1680728	69.6	1940017
68.01	363016	68.01	1773575	68.01	2136591
66.41	490857	66.41	1849428	66.41	2340285
64.83	630504	64.83	1906620	64.83	2537124
63.23	781206	63.23	1957476	63.23	2738682
61.63	929104	61.63	2000252	61.63	2929356
60.04	1070741	60.04	2032747	60.04	3103488
58.45	1193832	58.45	2059275	58.45	3253107
56.86	1305412	56.86	2077004	56.86	3382416
55.24	1404898	55.24	2094724	55.24	3499622
53.66	1487210	53.66	2106409	53.66	3593619
52.06	1565925	52.06	2118788	52.06	3684713
50.46	1637647	50.46	2131046	50.46	3768693
48.83	1674500	48.83	2138385	48.83	3812885
47.2	1727194	47.2	2149255	47.2	3876449
45.65	1792719	45.65	2160987	45.65	3953706
44.09	1840370	44.09	2172416	44.09	4012786
42.46	1924251	42.46	2190482	42.46	4114733
40.86	1983582	40.86	2206751	40.86	4190333
39.28	2050777	39.28	2230650	39.28	4281427

Continued

37.68	2105286	37.68	2246914	37.68	4352200
36.09	2166915	36.09	2269235	36.09	4436150
34.5	2226122	34.5	2295001	34.5	4521123
32.9	2281620	32.9	2317183	32.9	4598803
31.31	2346178	31.31	2347565	31.31	4693743
29.73	2413867	29.73	2378036	29.73	4791903
28.11	2469599	28.11	2414321	28.11	4883920
26.2	2494960	26.2	2423413	26.2	4918373
24.64	2543499	24.64	2452122	24.64	4995621
23.07	2599660	23.07	2482711	23.07	5082371
21.5	2656728	21.5	2520071	21.5	5176799
19.93	2716802	19.93	2561526	19.93	5278328

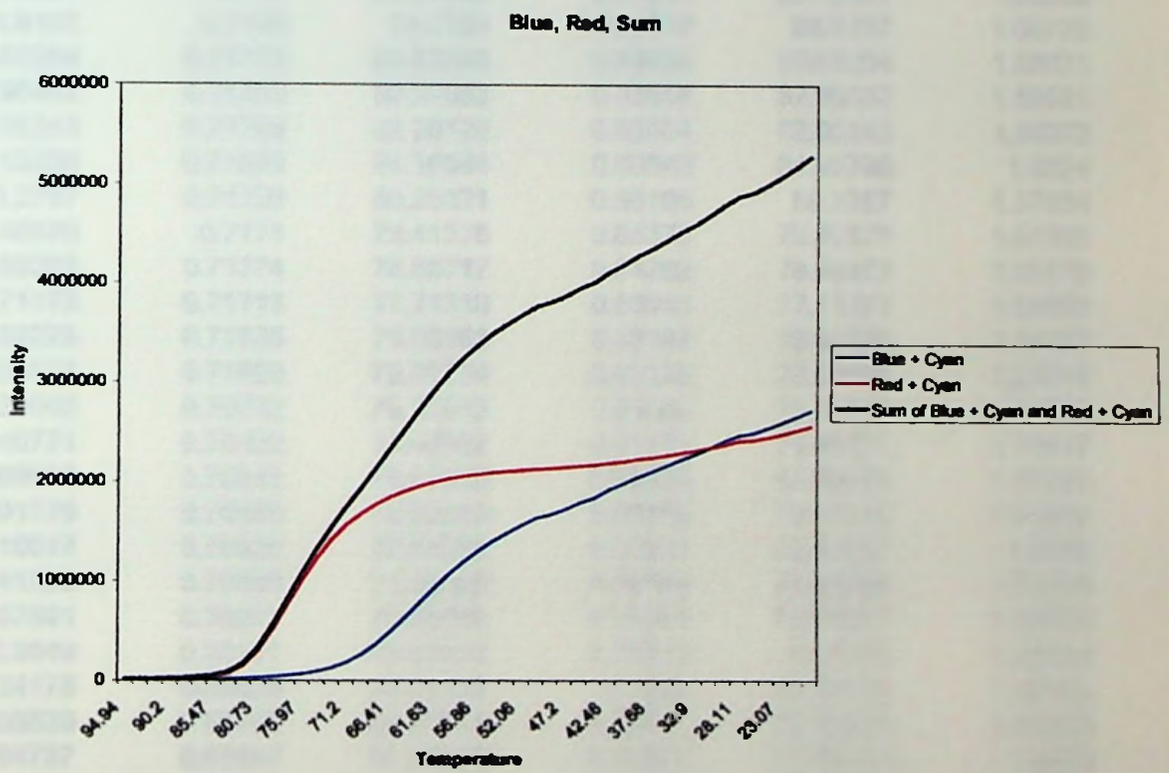

UV-Visible Spectroscopy Data

UV-Visible Data for Red + Cyan, Blue + Cyan and Numerical Sum

Temp °C	Red + Cyan	Temp °C	Blue + Cyan	Temp °C	Sum of Red + Cyan and Blue + Cyan
95	0.72595	95	0.87703	95	1.60298
93.91126	0.7154	93.91364	0.8755	93.91126	1.5909
92.83885	0.71607	92.8433	0.87482	92.83885	1.59089
91.78252	0.71541	91.78873	0.87227	91.78252	1.58768
90.74203	0.71634	90.7497	0.87309	90.74203	1.58943
89.71714	0.71765	89.726	0.87175	89.71714	1.5894
88.70763	0.71794	88.71738	0.87143	88.70763	1.58937
87.71325	0.71727	87.72363	0.87155	87.71325	1.58882
86.73379	0.71761	86.74452	0.87137	86.73379	1.58898
85.76901	0.718	85.77985	0.87038	85.76901	1.58838
84.8187	0.7168	84.8294	0.87042	84.8187	1.58722
83.88264	0.71713	83.89296	0.86958	83.88264	1.58671
82.96062	0.71703	82.97032	0.86818	82.96062	1.58521
82.05243	0.71768	82.06128	0.86604	82.05243	1.58372
81.15786	0.71698	81.16564	0.86542	81.15786	1.5824
80.2767	0.71736	80.28321	0.86198	80.2767	1.57934
79.40876	0.7171	79.41378	0.85373	79.40876	1.57083
78.55383	0.71774	78.55717	0.84702	78.55383	1.56476
77.71173	0.71718	77.71318	0.83965	77.71173	1.55683
76.88225	0.71695	76.88163	0.83197	76.88225	1.54892
76.06521	0.71609	76.06234	0.82135	76.06521	1.53744
75.26042	0.70732	75.25513	0.81569	75.26042	1.52301
74.46771	0.70462	74.45982	0.81155	74.46771	1.51617
73.68688	0.70642	73.67623	0.80739	73.68688	1.51381
72.91776	0.70569	72.90419	0.80325	72.91776	1.50894
72.16017	0.70529	72.14353	0.79951	72.16017	1.5048
71.41395	0.70389	71.39408	0.79796	71.41395	1.50185
70.67891	0.70271	70.65568	0.79564	70.67891	1.49835
69.9549	0.70111	69.92816	0.79413	69.9549	1.49524
69.24175	0.69925	69.21137	0.7926	69.24175	1.49185
68.53929	0.69788	68.50514	0.79047	68.53929	1.48835
67.84737	0.69847	67.80932	0.78873	67.84737	1.4872
67.16582	0.69283	67.12376	0.78729	67.16582	1.48012
66.49449	0.69009	66.44831	0.78596	66.49449	1.47605
65.83323	0.68739	65.78281	0.78363	65.83323	1.47102
65.18189	0.68347	65.12712	0.77756	65.18189	1.46103
64.54032	0.67981	64.4811	0.77664	64.54032	1.45645
63.90836	0.67558	63.84459	0.77991	63.90836	1.45549
63.28589	0.66972	63.21747	0.7789	63.28589	1.44862
62.67274	0.66675	62.5996	0.77794	62.67274	1.44469
62.0688	0.66284	61.99083	0.77766	62.0688	1.4405
61.47391	0.65979	61.39104	0.77705	61.47391	1.43684
60.88794	0.65681	60.80008	0.77548	60.88794	1.43229

60.31076	0.65398	60.21784	0.77397	60.31076	1.42795
59.74223	0.65103	59.64418	0.77309	59.74223	1.42412
59.18223	0.65002	59.07898	0.77257	59.18223	1.42259
58.63063	0.64729	58.5221	0.76973	58.63063	1.41702
58.0873	0.64604	57.97344	0.76796	58.0873	1.414
57.55212	0.64363	57.43286	0.76672	57.55212	1.41035
57.02496	0.6424	56.90025	0.76526	57.02496	1.40766
56.50571	0.6411	56.3755	0.76508	56.50571	1.40618
55.99425	0.6402	55.85847	0.76328	55.99425	1.40348
55.49046	0.63821	55.34907	0.76285	55.49046	1.40106
54.99422	0.63777	54.84718	0.76252	54.99422	1.40029
54.50542	0.63629	54.35268	0.76175	54.50542	1.39804
54.02396	0.63551	53.86548	0.76102	54.02396	1.39653
53.54971	0.63383	53.38545	0.76016	53.54971	1.39399
53.08258	0.63326	52.91251	0.75894	53.08258	1.3922
52.62245	0.632	52.44653	0.759	52.62245	1.391
52.16922	0.63121	51.98742	0.75752	52.16922	1.38873
51.72279	0.63095	51.53508	0.7574	51.72279	1.38835
51.28305	0.63017	51.08941	0.75697	51.28305	1.38714
50.84991	0.63019	50.6503	0.75697	50.84991	1.38716
50.42326	0.62878	50.21767	0.75681	50.42326	1.38559
50.00301	0.62805	49.79141	0.75632	50.00301	1.38437
49.58907	0.62543	49.37144	0.75725	49.58907	1.38268
49.18133	0.62401	48.95766	0.7556	49.18133	1.37961
48.7797	0.62328	48.54998	0.75523	48.7797	1.37851
48.3841	0.62334	48.14831	0.75545	48.3841	1.37879
47.99443	0.6221	47.75256	0.75435	47.99443	1.37645
47.61061	0.62175	47.36264	0.75392	47.61061	1.37567
47.23254	0.62135	46.97847	0.75195	47.23254	1.3733
46.86014	0.62109	46.59996	0.75087	46.86014	1.37196
46.49333	0.62062	46.22703	0.74974	46.49333	1.37036
46.13201	0.62018	45.8596	0.74977	46.13201	1.36995
45.77612	0.62019	45.49758	0.7491	45.77612	1.36929
45.42556	0.61942	45.1409	0.74933	45.42556	1.36875
45.08026	0.619	44.78948	0.74838	45.08026	1.36738
44.74014	0.61877	44.44324	0.74863	44.74014	1.3674
44.40511	0.61844	44.1021	0.748	44.40511	1.36644
44.07512	0.61827	43.76599	0.74818	44.07512	1.36645
43.75007	0.61804	43.43484	0.7478	43.75007	1.36584
43.42989	0.61758	43.10857	0.7478	43.42989	1.36538
43.11452	0.61693	42.7871	0.74791	43.11452	1.36484
42.80388	0.61716	42.47038	0.74696	42.80388	1.36412
42.49789	0.61674	42.15832	0.74673	42.49789	1.36347
42.1965	0.61736	41.85086	0.74696	42.1965	1.36432
41.89962	0.6174	41.54793	0.74712	41.89962	1.36452
41.60719	0.61671	41.24947	0.74675	41.60719	1.36346
41.31916	0.61649	40.95541	0.74725	41.31916	1.36374
41.03544	0.61404	40.66569	0.74698	41.03544	1.36102
40.75597	0.60939	40.38023	0.74562	40.75597	1.35501
40.4807	0.60954	40.09898	0.74611	40.4807	1.35565
40.20955	0.61322	39.82188	0.74586	40.20955	1.35908
39.94247	0.61345	39.54886	0.74532	39.94247	1.35877

39.6794	0.61319	39.27987	0.73923	39.6794	1.35242
39.42027	0.61333	39.01484	0.73875	39.42027	1.35208
39.16503	0.61305	38.75372	0.7426	39.16503	1.35565
38.91361	0.61327	38.49645	0.74312	38.91361	1.35639
38.66597	0.61298	38.24297	0.74338	38.66597	1.35636
38.42203	0.61327	37.99322	0.74355	38.42203	1.35682
38.18176	0.61296	37.74716	0.74364	38.18176	1.3566
37.94509	0.61339	37.50472	0.74312	37.94509	1.35651
37.71197	0.61316	37.26586	0.74297	37.71197	1.35613
37.48235	0.61285	37.03052	0.74344	37.48235	1.35629
37.25616	0.61267	36.79865	0.74283	37.25616	1.3555
37.03338	0.61247	36.57019	0.74265	37.03338	1.35512
36.81393	0.61038	36.34511	0.74232	36.81393	1.3527
36.59777	0.61009	36.12334	0.742	36.59777	1.35209

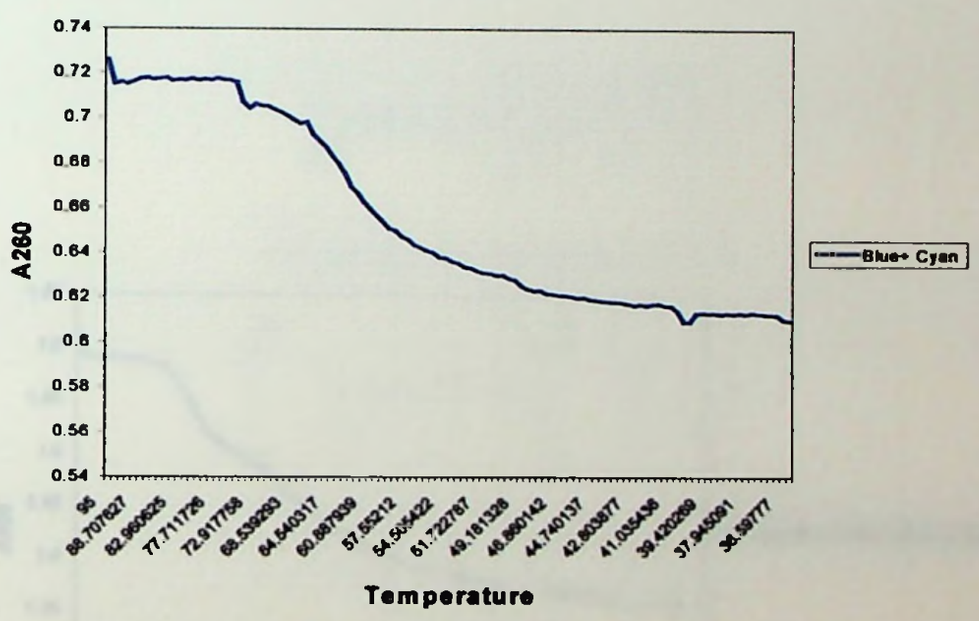

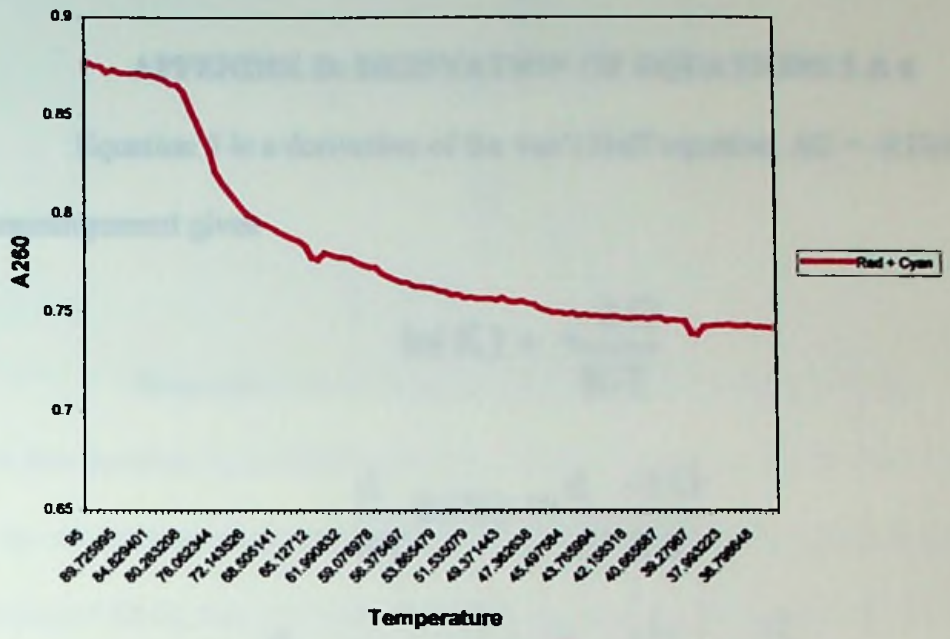
0.9
0.85
0.8
0.75
0.7
0.65
A260
Red + Cyan
95
89.725995
84.829401
80.283208
76.052344
72.143326
68.555141
65.12712
61.990832
59.078978
56.375497
53.865479
51.533079
49.371443
47.362658
45.497584
43.765994
42.159318
40.665587
39.27987
37.993223
36.798645
Temperature

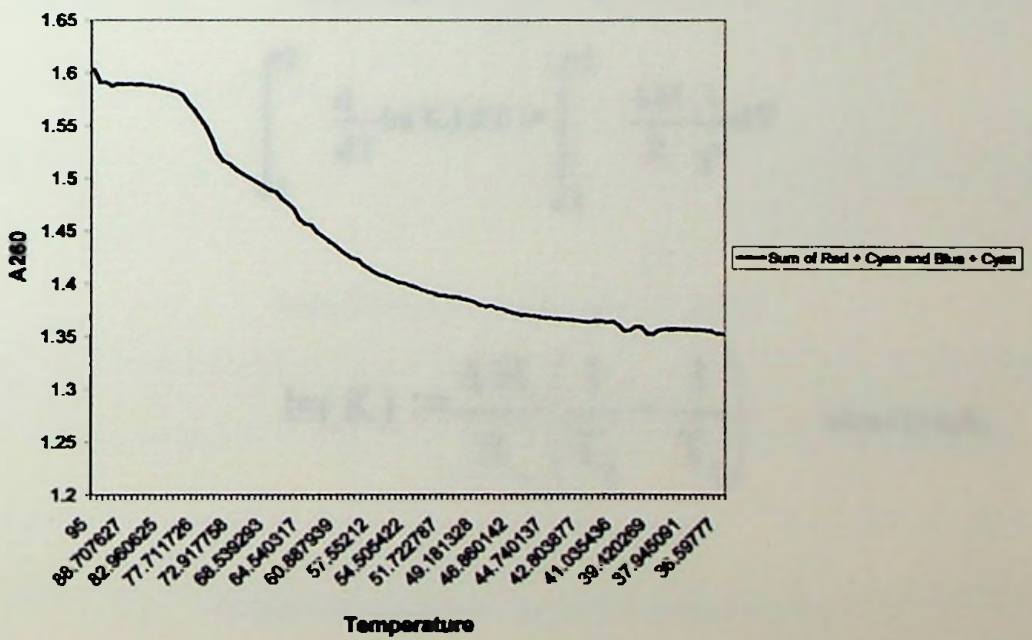
1.65
1.6
1.55
1.5
1.45
1.4
1.35
1.3
1.25
1.2
A260
Sum of Red + Cyan and Blue + Cyan
95
88.707627
82.960625
77.711726
72.917758
68.539283
64.540317
60.887939
57.55212
54.505422
51.722787
49.181328
46.860142
44.740137
42.803877
41.035436
39.420269
37.945091
36.59777
Temperature

APPENDIX D: DERIVATION OF EQUATIONS 5 & 6

Equation 5 is a derivation of the van't Hoff equation, $\Delta G = -RT\ln K$.

Rearrangement gives

$$\ln(K) = \frac{-\Delta G}{R \cdot T}$$

$$\frac{d}{dT}\ln(K) := \frac{d}{dT}\frac{-\Delta G}{R \cdot T}$$

$$\frac{d}{dT}\ln(K) := -\left[\frac{1}{R}\cdot\left(\frac{d}{dT}\frac{-\Delta H}{T} - \Delta S\right)\right]$$

$$\frac{d}{dT}\ln(K) := \left[\frac{1}{R}\cdot\left(\frac{-\Delta H}{T^2}\right)\right]$$

Integrating over the range of 1 to 2:

$$\int_1^2 \frac{d}{dT}\ln(K)\,dT := \int_1^2 \frac{\Delta H}{R}\cdot\frac{1}{T^2}\,dT$$

$$\ln(K) := \frac{\Delta H}{R}\cdot\left(\frac{1}{T_2} - \frac{1}{T_1}\right) \qquad \text{where } K = k_2/k_1$$

$$e^{\ln(K)} := e^{\frac{\Delta H}{R}\cdot\left(\frac{1}{T_2}-\frac{1}{T_1}\right)}$$

$$K := e^{\frac{\Delta H}{R}\cdot\left(\frac{1}{T_2}-\frac{1}{T_1}\right)}$$

Remember that K is an equilibrium constant equal to k_2/k_1.

In this instance, k_2 is equal to the rate of formation of annealed DNA, while k_1 is the rate of formation of single-stranded DNA. To determine the fraction, f, of annealed DNA, that amount must be divided by the total amount of DNA present.

$$f = k_2 / k_1 + k_2 .$$

Since the values of k_1 and k_2 are unknown, they may be derived through their relationship with K, so that $k_2 = K \times k_1$, and

$$k_1 = k_2 / K.$$

Substituting these values into f gives

$$f = \frac{K \cdot k_1}{K \cdot k_1 + \frac{K}{k_2}}$$

Simplifying the expression $\frac{K}{k_2}$ yields

$$f = \frac{K \cdot k_1}{K \cdot k_1 + \frac{1}{k_1}}.$$

Divide the numerator and denominator by k_1

$$\frac{K}{K+1}.$$

Substitute the value of K to yield the final equation:

$$f = \frac{e^{\frac{\Delta H}{R}\cdot\left(\frac{1}{T_2}-\frac{1}{T_1}\right)}}{e^{\frac{\Delta H}{R}\cdot\left(\frac{1}{T_2}-\frac{1}{T_1}\right)}+1}$$

where T_2 = Tm and the fraction, f, is fit to a function with the parameters T, Tm and ΔH.

In a two-process model, the fraction is the sum of two independent processes and so is described as

$$F(T, a, \Delta H, Tm) := \frac{e^{\left[\frac{\Delta H_1}{R}\cdot\left(\frac{1}{Tm_1}-\frac{1}{T}\right)\right]}}{1+\left[e^{\frac{\Delta H_1}{R}\cdot\left(\frac{1}{Tm_1}-\frac{1}{T}\right)}\right]} + \frac{e^{\left[\frac{\Delta H_2}{R}\cdot\left(\frac{1}{Tm_2}-\frac{1}{T}\right)\right]}}{1+\left[e^{\frac{\Delta H_2}{R}\cdot\left(\frac{1}{Tm_2}-\frac{1}{T}\right)}\right]}$$

However, this representation neglects the extent to which each process contributes to the fraction, or the overall process. To amend this, another parameter, a weighing factor denoted as **a**, is introduced. The value of a is an indicator of the effect which its accompanying parameter (Tm_2 for a, and Tm_1 for

1-a, for example) played in determining the final values obtained, as shown below in Equation 6.

$$F(T, a, \Delta H, Tm) := (1 - a_1) \cdot \frac{e^{\left[\frac{\Delta H_1}{R} \cdot \left(\frac{1}{Tm_1} - \frac{1}{T}\right)\right]}}{1 + \left[e^{\frac{\Delta H_1}{R} \cdot \left(\frac{1}{Tm_1} - \frac{1}{T}\right)}\right]} + a_1 \cdot \frac{e^{\left[\frac{\Delta H_2}{R} \cdot \left(\frac{1}{Tm_2} - \frac{1}{T}\right)\right]}}{1 + \left[e^{\frac{\Delta H_2}{R} \cdot \left(\frac{1}{Tm_2} - \frac{1}{T}\right)}\right]}$$

REFERENCES

1. Mirkin, Chad A. and Taton, Andrew. "Materials Chemistry: Semiconductors Meet Biology." *Nature* **405**, 626-627 (2000).
2. http://www.infras.com/Tutorial/sld005.htm
3. Cyanoski, David. "Japan Sets Sights on Success in Nanotechnology." *Nature* **408**, 624 (2000).
4. http://www.halcyon.com/nanojbl/NanoConProc/nanocan5.html
5. http://www.mitre.org/technology/nanotech/self_assembly.html
6. Ybe, Joel A. et al. "Clathrin Self-Assembly is Mediated by a Tandemly Repeated Superhelix." *Nature* **399**, 371-375 (1999).
7. MacGillivray, Leonard R. and Atwood, Jerry L. "A Chiral Spherical Molecular Assembly Held Together by 60 Hydrogen Bonds." *Nature* **389**, 469-472 (1997).
8. Casjens, S. Virus Structure and Assembly. Jones and Bartlett, Boston, 1995. pp. 75-147.
9. C. Mao, W. Sun, Z. Shen and N.C. Seeman, "A DNA Nanomechanical Device Based on the B-Z Transition." *Nature* 397, 144-146 (1999).
10. N. C. Seeman, "Nucleic Acid Nanostructures and Topology." *Angewandte Chemie*. 110, 3408-3428 (1998); *Angewandte Chemie International Edition* 37, 3220-3238 (1998).
11. N.C. Seeman, "DNA Nanotechnology: Novel DNA Constructions." *Annual Review of Biophysics and Biomolecular Structure* 27, 225-248 (1998).
12. E. Winfree, F. Liu, L. A. Wenzler, and N. C. Seeman, "Design and Self-Assembly of Two-Dimensional DNA Crystals." *Nature* 394, 539-544(1998).

13. N.C. Seeman, H. Wang, X. Yang, F. Liu, C. Mao, W. Sun, L. Wenzler, Z. Shen, R. Sha, H. Yan, M.H. Wong, P. Sa-Ardyen, B. Liu, H. Qiu, X. Li, J. Qi, S.M. Du, Y. Zhang, J.E. Mueller, T.-J. Fu, Y. Wang, and J. Chen, "New Motifs in DNA Nanotechnology." *Nanotechnology* 9, 257-273 (1998).

14. Braun, Erez et al. "DNA-Templated Assembly and Electrode Attachment of a Conducting Silver Wire." *Nature* **391,** 775-778 (1998).

15. Alivisatos, A. P. et al. "Organization of Nanocrystal Molecules Using DNA." *Nature* **382,** 609-611 (1996).

16. http://seemanlab4.chem.nyu.edu/cross.html

17. Barker, John. Marshall University Department of Chemistry, personal communication, Spring 2001.

18. Seeman, N. C. "*De Novo* Design of Sequences for Nucleic Acid Structural Engineering." *Journal of Biomolecular Structure and Dynamics* **8**, 573-581 (1990).

19. Rychlik, Wojciech. OLIGO Primer Analysis Software User Manual, 6th ed. Molecular Biology Insights, 2000.

20. van Holde, Kensal, Johnson, W. Curtis, and Ho, P. Shing. Principles of Physical Biochemistry. Upper Saddle River, NJ: Prentice Hall, 1998.

21. Harvey, David. Modern Analytical Chemistry. Boston: DePauw University, 2000.

22. Mathews, Christopher, van Holde, K. E., and Ahern, Kevin. Biochemistry, 3rd ed. San Francisco: Benjamin/Cummins, 2000.

23. *Methods in Enzymology* **19**, 395-397 (1974).

24. http://www.sosmath.com/diffeq/first/application/newton/newton.html

25. Ferragut, C. and Leclerc, H. "Etude Comparative des Methodes de Determination du Tm de l'and Bacterien." *Ann. Microbiol. (Inst. Pasteur)* **127A**, 223-235 (1976).

26. Lakowicz, Joseph C. Principles of Fluorescence Spectroscopy. New York: Plenum Press, 1983.

27. Molecular Probes, Inc. Product Information MP 07567

28. Mason, W.T., ed. Fluorescent and Luminescent Probes for Biological Activity, 2nd ed. London: Academic Press, 1999.

29. ThermoMicroscopes Corporation. Practical Guide to Scanning Probe Microscopy. Sunnyvale, CA: ThermoMicroscopes Corporation, 1996-2000.

30. Marek, Tony, ed. ThermoMicroscopes Explorer Instrument Operation Manual. Sunnyvale, CA: ThermoMicroscopes Corporation, 2000.

31. http://www.asmicro.com/phase.htm

32. Manner, William L. Union Carbide Corporation Technical Center, personal communication, July 2000.

33. Li, X. J. et al. "Antiparallel DNA Double Crossover Molecules as Components for Nanoconstruction." *Journal of the American Chemical Society*, 118, 6131-6140, 1996.

34. Thomson, N. H. et al. "Reversible binding of DNA to mica for AFM imaging." *Langmuir* **12**, 5905-5908, (1998).

35. Allen, M. J. et al. "AFM Analysis of DNA-Protamine Complexes Bound to Mica." *Nucleic Acids Research* **25**, 2221-2226, (1997).

36. Bonnell, Dawn A., ed. Scanning Tunneling Microscopy and Spectroscopy: Theories, Techniques, and Applications. New York: VCH, 1993.

37. Ewbank, Nathan J. and Creighton, Thomas E. "Protein Folding by Stages," *Current Biology* **2**, 347-349 (1992).

38. Martin, J. and Hartl, F. "Molecular Chaperones in Cellular Protein Folding," *Bioessays* **16**, 689-692 (1994).

39. Huheey, James E., Keiter, Ellen A., and Keiter, Richard L Inorganic Chemistry: Principles of Structure and Reactivity, 4th ed. New York: HarperCollins, 1993.

40. Hicks, Leslie and Price, William. "Questions of Life and Death Explored in the Physical Chemistry Lab: How and Why Proteins Fold." 223rd ACS National Meeting, Spring 2000.

41. Primerano, Don. Joan C. Edwards School of Medicine Department of Molecular Biology, personal communication, July 2001.